R-14-12

Spalling initiation experiments on large hard rock cores

Lars Jacobsson, Karin Appelquist, Jan-Erik Lindqvist
RISE Research Institutes of Sweden

Urban Åkesson, Swedish Transport Administration

February 2018

Svensk Kärnbränslehantering AB
Swedish Nuclear Fuel
and Waste Management Co

Box 3091, SE-169 03 Solna
Phone +46 8 459 84 00

ISSN 1402-3091
SKB R-14-12
ID 1597538

February 2018

Spalling initiation experiments on large hard rock cores

Lars Jacobsson, Karin Appelquist, Jan-Erik Lindqvist
RISE Research Institutes of Sweden

Urban Åkesson, Swedish Transport Administration

Preface

The work in this report has been initiated and funded by the Swedish Nuclear Fuel and Waste Management Co (SKB) which is responsible for the disposal of used nuclear fuel in Sweden. The nuclear fuel is intended to be stored some hundreds of meters below surface level in facilities built in high strength rock. The in situ rock stress may cause unwanted rock spalling in tunnels and drilled deposition holes, which is one of the aspects in the safety assessment analysis carried out by SKB in conjunction with the on-going repository design.

The design of the experiments was discussed with Rolf Christiansson, SKB and Derek Martin, University of Alberta, Canada. The tests were carried out during April and May 2009 at the rock mechanics laboratories at SP Technical Research Institute of Sweden. The post characterization of the fractures was carried out at the Swedish Cement and Concrete Research Institute during the end of 2010.

SP Technical Research Institute of Sweden and Swedish Cement and Concrete Research Institute have since the work was carried out changed name to RISE Research Institutes of Sweden.

Abstract

A new type of laboratory test method to determine spalling resistance in a situation as in large boreholes in hard rock has been demonstrated. Uniaxial compression tests on large cores with notches were conducted on Äspö diorite from Äspö HRL. Spalling was localized to the notches where the local stress was highest. The crack initiation, crack coalescence and crack damage stresses representing various fracture stages were identified by using acoustic emission monitoring with source localization. The actual stress levels were obtained from the axial forces at which the various fracture stages were identified via FE-calculations representing the actual specimen geometry and loading. The results were compared with uniaxial compression tests carried out on cores with standard size on the same rock type also from Äspö HRL.

The results showed that spalling chips were formed similar to those found in field which indicates that the test is representing a realistic behaviour. However, the results show that the various fracture stress levels found in the tests are higher than the spalling strength found in the field and in the test of small cores. The higher stress levels could be caused by a number of reasons described in the report.

A post characterization of the fractures was carried out on slabs that were cut out from the specimens containing the notch areas. The occurrence of microcracks and how they have propagated through the different minerals and the location in relation to the notches, minerals and grain boundaries were investigated. The patterns of the major fractures and the secondary fractures were analysed. The majority seem to be extension fractures, but shearing could also be verified. The results from the microscopy analysis provide invaluable information of the spalling process at all stages.

Sammanfattning

En ny typ av laboratorieprovmetod för att bestämma spjälkningsmotstånd i en situation som i stora borrhål i hårt berg har demonstrerats. Enaxiella kompressionsförsök på stora kärnor med notchar (urtag) genomfördes på Äspödiorit från Äspö HRL. Spjälkning lokaliserades till notcharna där den lokala spänningen var högst. Sprickinitierings-, spricksammanslagnings-, och sprickskadespänningen som representerar olika sprickstadier identifierades genom att använda akustisk emmissionsmätningar med lokalisering av källan. De aktuella spänningsnivåerna erhölls från den axiella kraften som de olika sprick stadierna identifierades via FE-beräkningar som representerar det aktuella provets geometri och belastning. Resultaten jämfördes med enaxiella kompressionsförsök som genomförts på borrkärnor med standardstorlek och bergart också från Äspö HRL.

Resultaten visade att spjälkningsbitar bildades liknande sådana som funnits i fält vilket indikerar att provet representerar ett realistiskt beteende. Emellertid visar resultaten att spänningarna vid de olika sprickstadierna i proven är högre än spjälkningshållfastheten som man har funnit i fält och i proven av de små kärnorna. De högre spänningsvärdena kan bero på ett antal orsaker som beskrivs i rapporten.

En post-karaktärisering av sprickorna genomfördes på skivor som sågades ut från proverna innehållande notch-områdena. Förekomsten av mikrosprickor och hur de har växt till genom de olika mineralerna och deras läge i förhållande till notcharna, mineralerna och korngränserna undersöktes. Mönstren av de huvudsakliga sprickorna och de sekundära sprickorna analyserades. Merparten verkar vara dragsprickor men skjuvning kunde också påvisas. Resultaten från mikroskopiundersökningarna ger ovärderlig information om spjälkningsprocessen vid alla stadier.

Contents

1 Introduction

1.1 Background

Spalling in rock takes place in tunnels and boreholes caused by the in situ rock stress. A fundamental issue is to be able to predict at which stress level spalling is initiated as this is important for the design and stability of underground constructions and boreholes. Field observations and experiments (e.g. Martin 1993, Andersson 2007, Edelbro 2008) have provided an understanding of the initiation and development of spalling. However, field experiments are cumbersome and expensive to conduct. Moreover, they are subjected to a number of uncertainties such as the actual in situ stress state and the homogeneity of the rock mass. Different types of laboratory experiments have therefore been proposed for investigating the spalling initiation.

Uniaxial compression tests have been conducted in which the onset of when the inelastic part of the volumetric strain, also called crack volume strain, $\varepsilon_{vol,cr} = \varepsilon_{vol} - \varepsilon_{vol,el}$, displays a dilation has been used as an indicator for spalling initiation, cf. e.g. Martin (1993), Eberhart (1998), and Hakala and Heikkilä (1997). Moreover, Eberhart (1998) carried out AE-measurements together with volumetric strain measurements to determine the crack initiation stress in order to compare the values from both methods. The elastic part of the volumetric strain $\varepsilon_{vol,el}$ is computed using the values of the elastic constants Young's modulus and Poisson ratio. This introduces an uncertainty as the values of the elasticity constants have a variability due to the specific chosen criterion for the evaluation. This is one of the drawbacks with the volumetric strain method. Another drawback is that it can be difficult to determine the onset of dilation for the crack volume strain as it requires filtering of data and a judgement of when dilation starts. The latter issue is addressed by Eberhart (1998) and Hakala and Heikkilä (1997). Diederichs et al. (2004) have further determined the various stages during the crack development, by using strain and AE measurements. Moreover, they introduce a field strength ratio ($FSR = UCS_{in\ situ}/UCS_{lab}$) which depends on the rock type, grain size, foliation and fractures, mineralogy and minor minerals and phyllosilicates. Martin and Christiansson (2009) suggest that the in situ spalling strength is about 0.4–0.5 of UCS for hard rock.

The "hole in a plate" test is a test where a rock block or plate is compressed in one direction in order to accomplish a tangential stress in the hole which causes spalling. Martin (1993) and Martin et al. (1994) summarize the results from a number of tests, see Figure 1-1. It is seen that the ratio between the tangential stress and UCS is decreasing with increasing borehole diameter. The ratio is approaching 0.8–1 for diameters of 75–115 mm. Diederichs et al. (2004) discuss the effect of feedback confinement which suppress the spalling both in the case of uniaxial compression and in the hole in the plate test. This is illustrated in Figure 1-2.

A biaxial plane strain test was proposed by Labuz et al. (1996). The specimen, which is prismatic, is biaxially loaded, whereby plane extension fractures will initiate on the unloaded free face in the third direction. Labuz et al. (1996) carried out tests on sandstone. One difficulty with that test is to apply the biaxial stress without having friction forces on the faces which makes the stress state not well defined.

To this date there is still no laboratory test method that fully resembles the spalling in tunnels and boreholes in an appropriate manner.

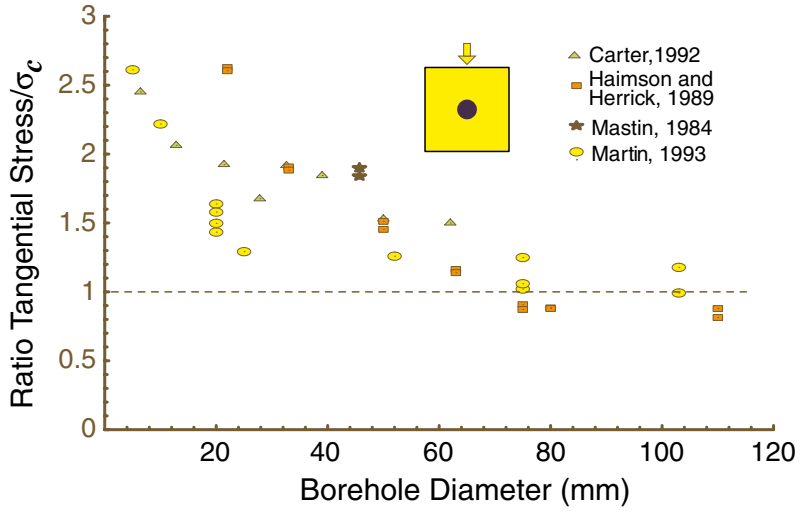

Figure 1-1. *Results from different hole in a plate test showing the ratio between the tangential stress when fracturing starts and UCS for various borehole diameters. From Martin et al. (1994).*

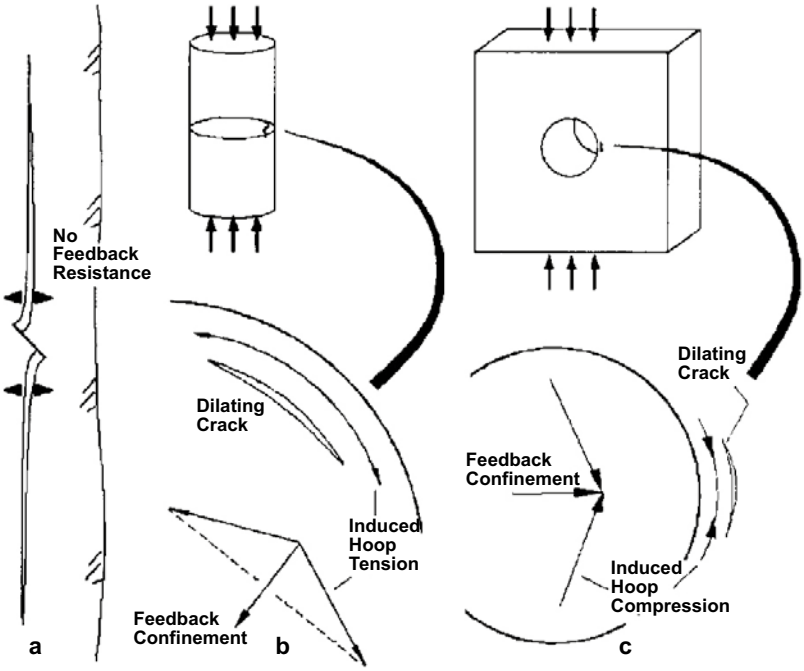

Figure 1-2. *Illustration of feedback confinement for different cases. From Diederichs et al. (2004).*

1.2 Aim and scope

There is a need of a laboratory test method in which controlled and repeatable tests can be conducted to determine the spalling initiation stress for a set-up that can resemble the conditions in deposition boreholes with a diameter of about 1.8 m. The aim of this work was to see how well the new type of laboratory test set-up can resemble a realistic spalling behaviour.

The specimens should be large enough in relation to the microstructure of the rock such that the local stress state at the spalling area will be representative for the in situ case. Moreover, the specimen size is important from another point of view, i.e. regarding the loaded volume or area. The critically loaded volume, i.e. where spalling is anticipated, will be large on a large specimen. This means that there is a higher probability that inherent weak areas in the rock material will be critically loaded during the experiments. The inherent weak locations are constituted by defects or flaws which may be material inclusions, large grains or small cracks.

This report contains results from spalling tests on large cores and a post-characterization of the fractures in the spalling zone by means of microscopy techniques. Appendix A contains results from uniaxial compression tests on small cores used as a reference to ordinary investigation methods of the spalling behaviour.

1.3 Ideas of the proposed new spalling test

One of the three principal stresses at a deposition hole is approximately oriented such that the stress directed along the borehole is small (σ_V). The other two principal stresses are perpendicular to the borehole (σ_h and σ_H), cf. Figure 1-3. Note that the orientation of the tunnel axis relative to the orientations of σ_h and σ_H can be arbitrary and the tunnel orientation shown in Figure 1-3 is only for illustration of one conceptual case. Looking at the wall of the deposition hole, the resulting largest compressive stress is called the tangential stress (σ_t) and is the stress component that will cause spalling. The stress in the radial direction (σ_r) is zero at the surface. Both σ_t and σ_r changes the value further into the wall (rock mass); σ_t decreases and σ_r increases (becomes compressive).

The idea behind the test is to resemble the stress state in the direction of the tangential stress by taking out a specimen as shown in Figure 1-4, were maximum in-situ stress (horizontal) is σ_H. The specimen will be axially loaded and will contain a part of the borehole. In our case, we will use specimens from large cores in which two notches are manufactured opposite to each other in order to obtain a correct representation of the local stress state, see Figure 2-2. Two notches will be manufactured in order to obtain symmetry during loading to avoid bending which may endanger the test.

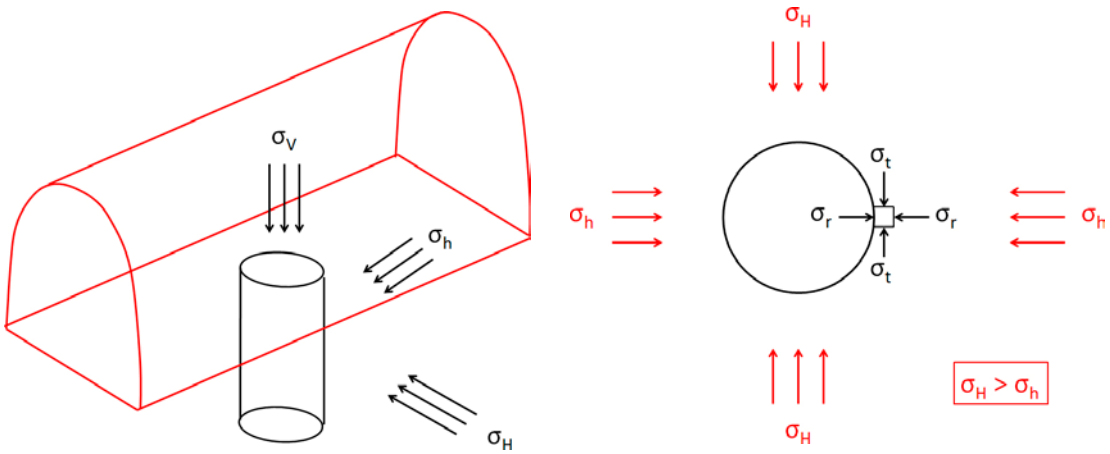

Figure 1-3. *Schematic picture of the stress field around a deposition hole at the APSE experiment site (Anderssson, 2007). The access tunnel is illustrated in red. Left: Far-field stresses (σh , σH and σV); Right: Stresses at the wall of the deposition hole seen from the top (σt and σr).*

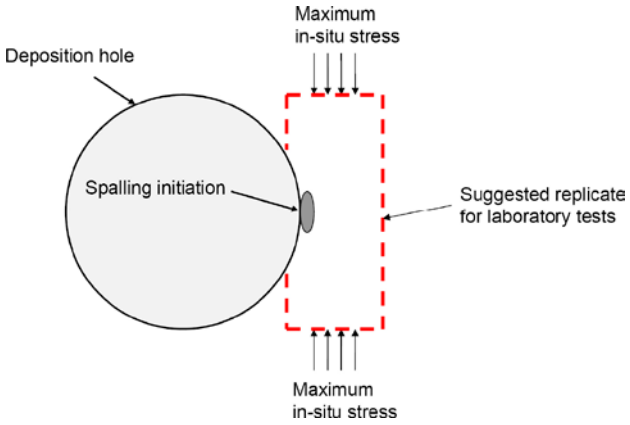

Figure 1-4. *Illustration of the idea behind the test.*

2 Uniaxial compression tests on notched large specimens

2.1 Test material

Three cores of intact rock were sent to SP which arrived at SP during January 2009. The borehole information and geometrical data of the cores are given in Table 2-1. The lengths are given as the part of the cores which has a full diameter. One core arrived broken into two pieces. The rock type was Äspö diorite which has large feldspatic phenocrysts (up to 25 mm size and more of K-feltspar) which yields a heterogenic material. The material structure can be seen in Figure 2-1. It is also seen that the cores contains sealed joints (especially KS0037B02). Core KS0044B02 has a large mafic enclave (amphibolite) in a form of a thick band. This part of the specimen will not be used in the test.

It was judged that the sealed joints in core KS0037B02 may affect the spalling initiation and the core was instead decided to be used for uniaxial compression tests on small diameter cores as a reference, see Appendix A. The small diameter specimens were drilled out from the large core.

Table 2-1. Specimen identification, sampling level (borehole length) and rock type for all specimens (based on the Boremap). The position was written on the core boxes.

Identification	Diameter (mm)	Length (mm)	Position (m)	Rock type/occurrence
KS0037B02	241	c 500 + 300	0.87–1.92	Äspö diorite
KS0041B02	241	c 450	10.90–11.45	Äspö diorite
KS0044B02	241	c 800	unknown–0.95	Äspö diorite

Figure 2-1. *Specimens after they arrived to SP. Upper picture: KS0037B02; Middle picture: KS0041B02; Lower picture: KS0044B02. The surfaces of the cores were moistured in order to better reveal the rock texture.*

2.2 Specimens

2.2.1 Geometry

Specimens with two plane single curved notches opposite to each other are proposed for KS0041B02 and KS0044B02 in order to localize the spalling to the notch. The notch geometry was chosen to reflect the loading situation in a borehole, cf. Section 1.3. The notch radii were designed such that the stress amplification in the axial direction was about 1.7 times the nominal axial stress in the specimen and for keeping the symmetry reducing the risk for an unwanted specimen failure due to bending. The axial stress at the centre of the specimen between the notches is about 1.2 times the nominal stress. The nominal stress is the axial force divided by the full circular cross section area in the un-notched part of the specimen. The notch centre is shifted 50 mm in the specimen axial direction in order to obtain an un-notched area which could be used to determine the nominal stress-strain relation for the cores. The final specimen dimensions are shown in Figure 2-2.

A finite element model was set-up for specimen KS0044B02 using a linear elastic material representation to later be able to compare measured deformation values with calculated ones. The values of the elasticity constants were set to E = 66 GPa and ν = 0.34. These values were estimated based on other test results on the Äspö diorite, see Appendix A. An axial prescribed displacement of 0.00783 mm giving a nominal stress 1.0 MPa was applied which yields a total reaction force of 45.7 kN. The calculated stress state in the most stressed area in the notch was

$\sigma_{11} = \sigma_{mid} = 0.08$ MPa
$\sigma_{22} = \sigma_{min} = 0.04$ MPa
$\sigma_{33} = \sigma_{max} = 1.7$ MPa

where σ_{11} is directed across the notch, σ_{22} is normal to notch surface and σ_{33} is in the specimen axial direction. The σ_{min}, σ_{mid} and σ_{max} are the principal stresses. The σ_{22}-stress component should theoretically be zero at the centre of the notch. The non-zero value is due to that the element stresses obtained in the integration points located under the specimen surface were extrapolated to nodal stress values at the surface. Moreover, the centremost node is not exactly located in the centre of the notch.

Note that all the computed values are linearly scalable due to the use of a linear model of the specimen. This will be used later on in this report. Contour plots of the stress distributions are shown in Figure 2-3.

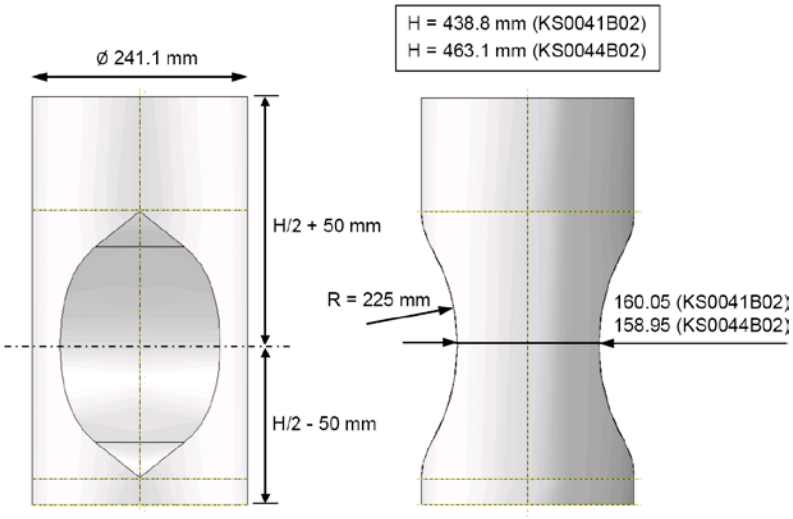

Figure 2-2. *Specimen geometry.*

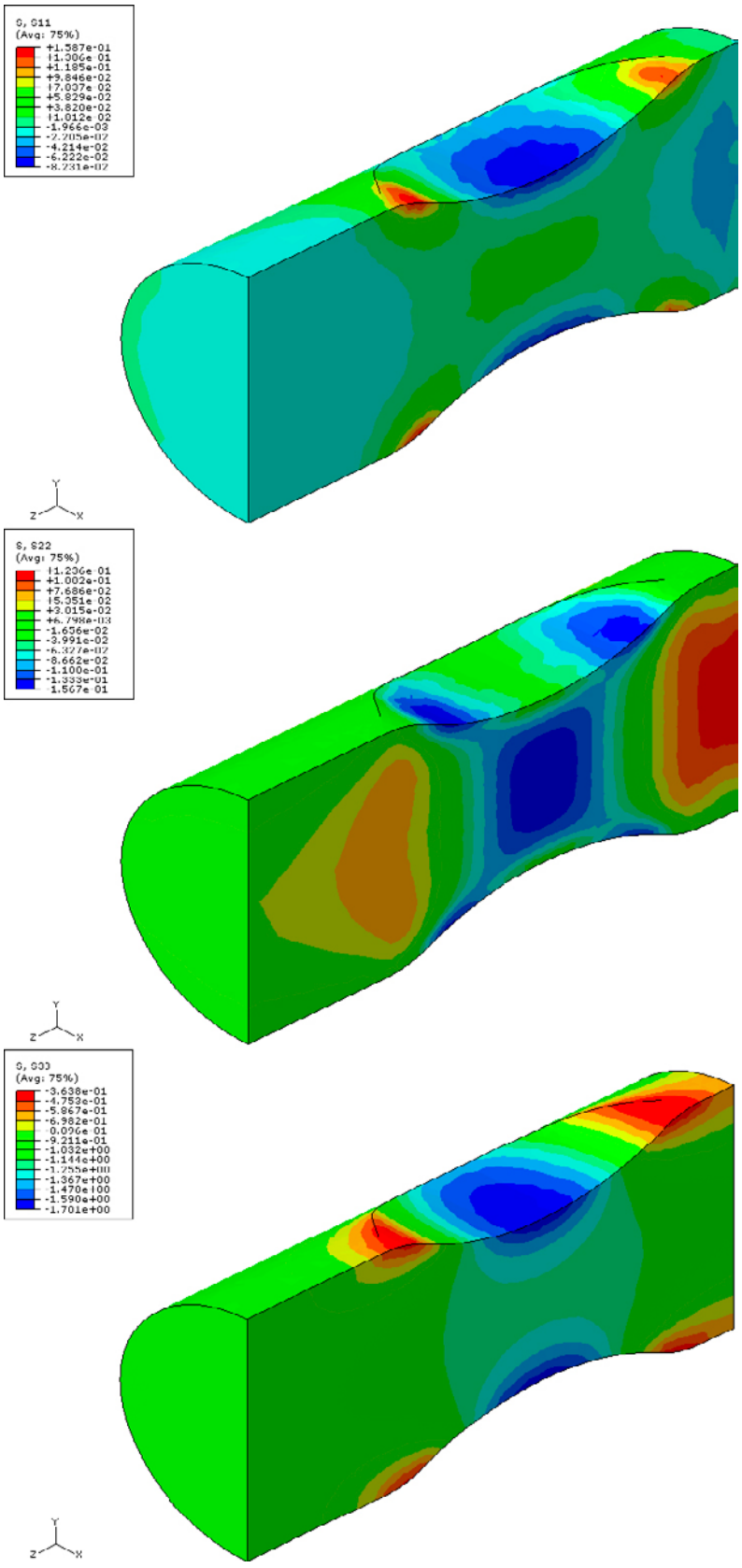

Figure 2-3. *Stress distributions in the specimen at a nominal axial stress of 1.0 MPa.*

2.2.2 Manufacturing

Two cylindrical specimens were manufactured from the cores, KS0041B02 and KS0044B02. The end surfaces were grinded and two plane single curved notches with smooth surfaces were manufactured opposite to each other. The notch is shifted 50 mm in the specimen axial direction. Pictures of the specimens after manufacturing are shown in Figures 2-4 and 2-5. It is seen that specimen KS0044B02 has a large xenolith of fine grained mafic rock material in the centre of the notch on side one.

Figure 2-4. *Specimen KS0041B02. Sides 1–4. The surface has been slightly grinded in the darker areas on the top of the specimen for subsequent strain gauge installation.*

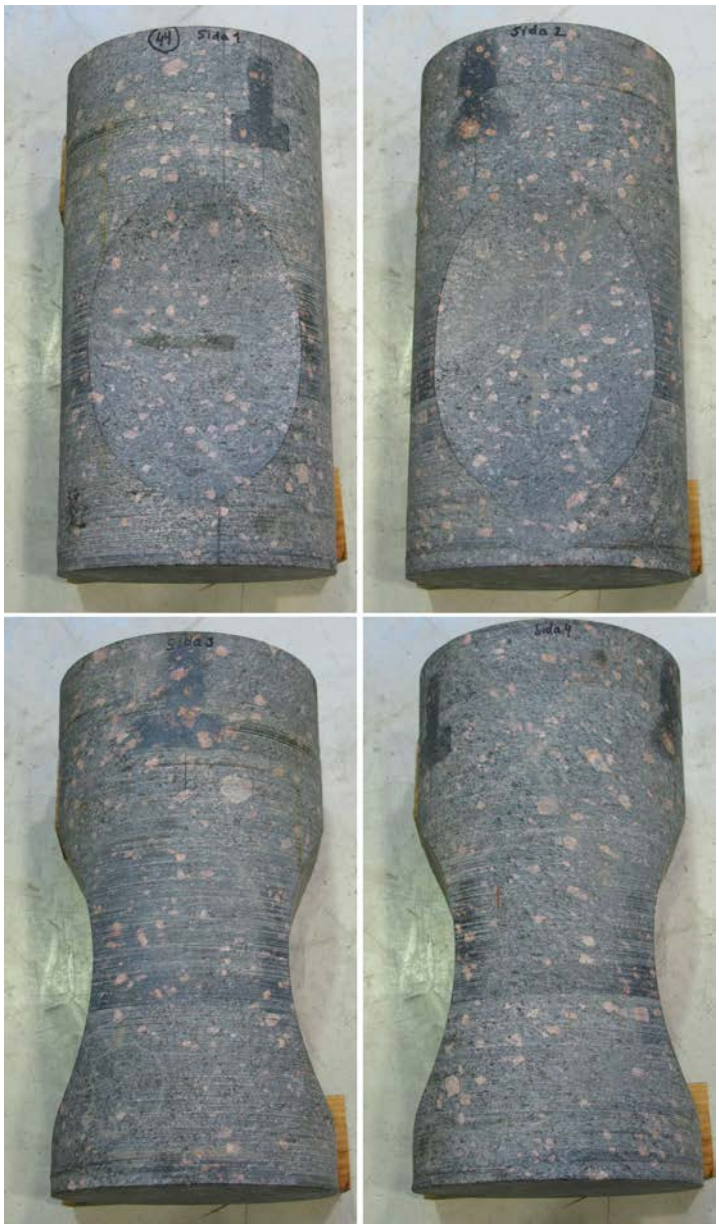

Figure 2-5. *Specimen KS0044B02. Sides 1–4. The surface has been slightly grinded in the darker areas on the top of the specimen for subsequent strain gauge installation. A long mafitic xenoliths in the horizontal direction is seen at the centre on the notch on side 1 (upper left figure).*

2.3 Test set-up

2.3.1 Loading device

A four column load frame with a maximum compressive load of 20 MN was used for the tests, see Figure 2-6. A safety assessment was carried out prior to the test start. As a result of this, the area where the supervision of the test was carried out was sealed off by a wall of concrete blocks in the case of a specimen failure, see Figure 2-7. The specimen was loaded between flat loading platens of hardened steel. A spherical seat was placed over the upper loading platen. The load was initially measured using an electrical load cell rated up to 5 MN. This would yield a maximum tangential stress of 186 MPa in the notch according to FE-simulations which was estimated to be enough force to achieve spalling. The electrical load cell was subsequently removed as it turned out that fully developed spalling did not take place at a load of 5.0 MN during the first test (KS0041B02). After that, the load was measured only by means of the hydraulic pressure.

Figure 2-6. *Specimen KS0044B02 placed in the load frame right before testing. The concrete blocks sealing off towards the control area are seen in the background.*

Figure 2-7. *Control and monitoring area during the tests behind the protection shield.*

2.3.2 Specimen instrumentation

One- and two-directional foil strain gauges (30 mm and 10 mm gauge length) from Kyowa were installed on the two specimens. The 30 mm gauge length was judged to be suitable for the relatively coarse grained material in order to achieve an average strain value. The two-directional strain gauge was chosen with 10 mm gauge length as this was the largest available gauge length for this type.

The one-directional strain gauges were placed both in the axial and circumferential direction with a 120 degrees division on the cylindrical part of the specimen in order to monitor the homogeneous uniaxial deformation behaviour. Besides this, another set of one-directional strain gauges were placed just outside the notches and one additionally was placed exactly in the centre of the notch on one of the notches on each of the two specimens. Finally, a two-directional strain gauge was placed 20 mm to the left of the centrally mounted one-directional strain gauge in order to measure the axial and transverse strain.

Four acoustic emission sensors were placed on the specimen during the test. Two types of sensors were used with 60 and 150 kHz peak sensitivity. The 60 kHz sensors (AE1 and AE2) were placed on one side of the specimen and the 150 kHz sensors (AE3 and AE4) on the opposite side, right above and under the notches. The use of four sensors allows for localization of the recorded acoustic events.

The total axial deformation of the specimen was measured by means of three linear displacement transducers (LDT) which were attached to the upper and lower loading platen, respectively, with a 120 degrees division around the specimen.

The locations of the sensors are shown in Figure 2-8 and 2-9.

The strain gauges were checked using a shunt resistance prior to the tests. The linear displacement transducers were calibrated using gauge blocks, see Figure 2-10. The signals from the load cell, strain gauges and linear displacement gauges were sampled using a HBM MGCplus device.

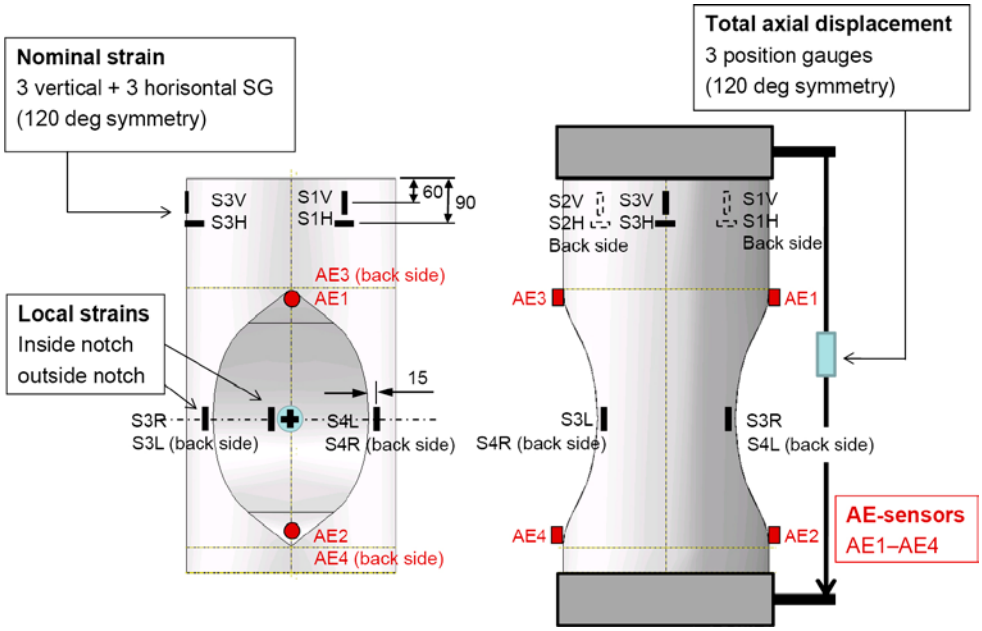

Figure 2-8. *Placement of the strain gauges (S) and acoustic emission sensors (AE) for specimen KS0041B02. The total axial deformation measurement is visualized in the right figure where the sensors are connected to the upper and lower loading platens. The strain gauges for local measurements and AE-sensors have switched sides on specimen KS0041B02.*

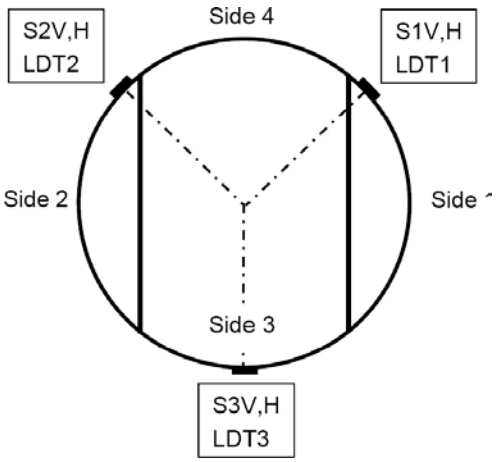

Figure 2-9. *Specimen seen from the top with the placement of the strain gauges (S) and total axial deformation measurement (LDT).*

Figure 2-10. *Calibration check of the LVDTs by means of gauge blocks (Johansson gauge) prior to the test of KS0041B02.*

2.3.3 Test scheme

The specimens were put in a stainless steel vat tub and the vat tub was filled with tap water such that the specimens were completely covered with water, see Figure 2-11. The specimens were stored in water until the time for the testing in order to obtain a water content resembling the in situ conditions. Specimen KS0041B02 was stored in water for 13 days and KS0044B02 for 15 days. The obtained degree of water saturation was not checked. The overall test procedure is shown in Table 2-2. There are some small differences in the test procedure between the tests of the two specimens. The differences are described in Sections 3 to 5 in conjunction with results of the individual tests.

Table 2-2. Activities during the mechanical testing.

Step	Activity
1	The specimen was put in place and centred between the loading platens.
2	Mounting the linear displacement transducers, AE-sensors and connect the strain gauges.
3	Check the calibration of the linear displacement transducers and the strain gauges.
4	Check / adjust the sensitivity of the AE-sensors.
5	Moisture the surfaces of the specimens.
6	Preload the specimen.
7	The centring was checked again.
8	The deformation and strain measurement channels were zeroed.
9	The loading was started with an loading rate which was lowered when the assumed limit of spalling initiation was approachning.
10	The test was stopped when the recorded AE-events yielded strong and very dense signals proving that significant fracturing were taking place.
11	The specimens was unloaded.
12	Digital photos were taken on the specimen after the mechanical testing.

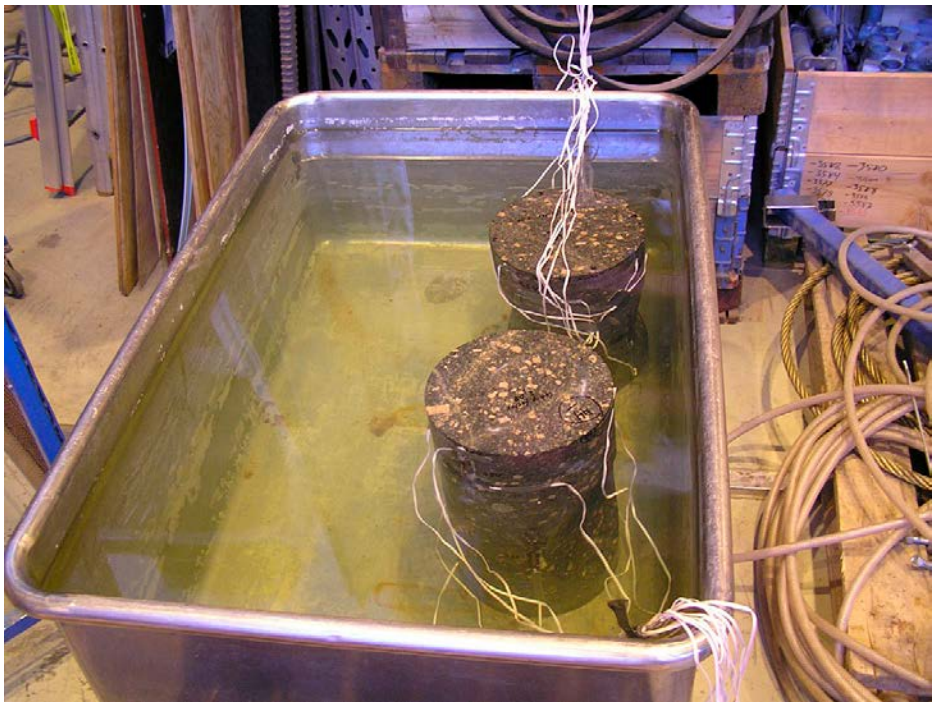

Figure 2-11. *Specimens stored in water prior to testing in a stainless steel vat tub.*

3 Test of KS0041B02 (first load cycle, 0–5.0 MN)

3.1 Procedure

The test was conducted according to Table 2-2. The surface of the specimen had a time to dry for about 4 hours while installing the specimen and setting up the measurement devices. Water was sprayed on the surface some minutes before the test in order to re-moisture the surface before the loading started. The specimen was not further moistured during the test.

The specimen was manually pre-loaded up to 0.1 MN in order to settle all contacts. The initial loading rate from 0.1 MN was 0.08 MN/min up to 2.8 MN. The load rate was then significantly decreased as spalling was expected to occur close to this load level. The load level was then increased stepwise up to 0.03 MN/min which was kept until 5.0 MN which was the maximum load for the electrical load cell. No significant spalling did occur so far. The specimen was then unloaded and put back into water. The actual load rates for the test are shown in Figure 3-1.

3.2 Total deformations

The axial force versus the total deformation measurements are shown in Figure 3-2. The curves from measurements are showing a slightly wavy behaviour. The linear displacement transducers were attached on the upper loading platens with their measuring tips pointing down on bars which were attached on the lower loading platens, see Figure 2-10. It is likely that the tips of the linear displacement gauges have moved a little sideways relative to the plane surfaces on the end of the bars. The end surfaces have some roughness which could introduce the waviness.

The average value of the three linear displacement transducers at the maximum load was 0.833 mm. This can be compared with a computed value of 0.857–0.040 = 0.816 mm. The computed value is the value from the FE-simulation of the KS0044B02 specimen adjusted due to that the KS0041B02 specimen was somewhat shorter than the KS0044B02 specimen.

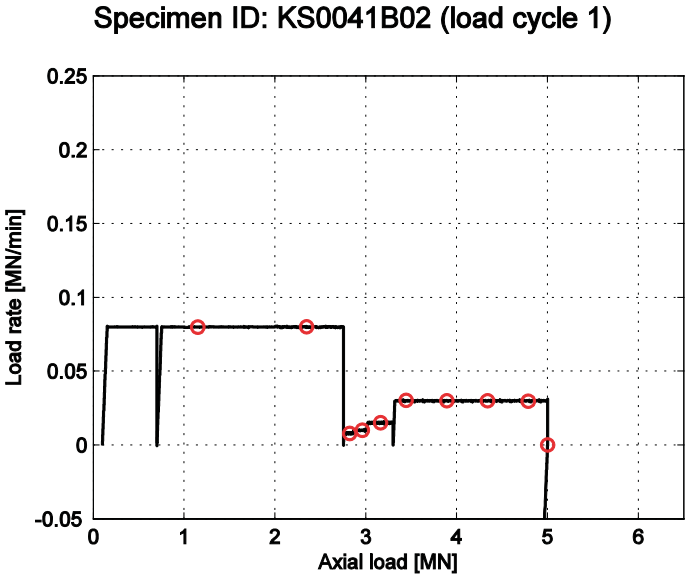

Figure 3-1. *The load history during the first load cycle on specimen KS0041B02. The red circles mark every15 minutes test time.*

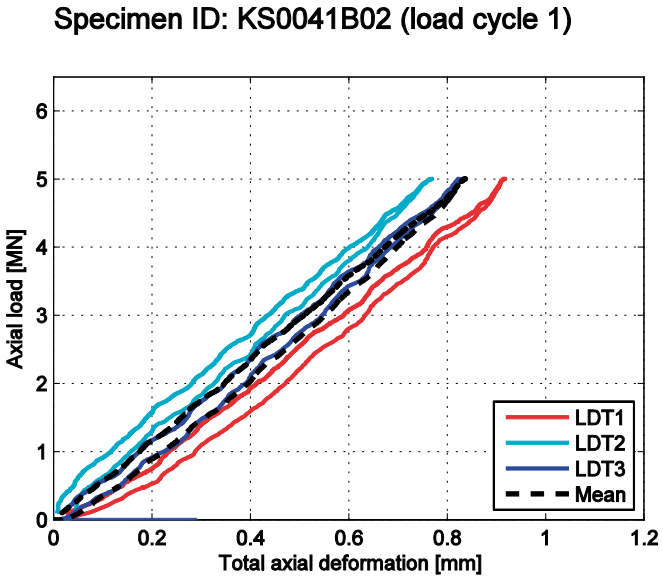

Figure 3-2. *Total axial deformation during the first load cycle on specimen KS0041B02 recorded by the three linear displacement transducers (LDT) and their mean value.*

3.3 Nominal strains and strains in the notch

The nominal stress versus strain in the cylindrical upper part of the specimen is shown in Figure 3-3. The thick dashed lines (Mean) show the mean values of the measurements in the axial and circumferential direction. The values of the elasticity constants were E = 65.4 GPa and ν = 0.36. The constants were evaluated as the secant value between 90 MPa and 109.6 MPa ($\sigma_{a,max}$).

The recorded strains in the notch area are shown in Figure 3-4. The recorded strains at the maximum load were 0.30 % in the vertical 30 mm strain gauge at the centre of the notch and 0.31 % respective –0.082 % in the two-directional strain gauge. The Poisson's ratio measured by the two-directional strain gauge yields a value of 0.34 evaluated as the secant value between 80 % and 100 % of the maximum load.

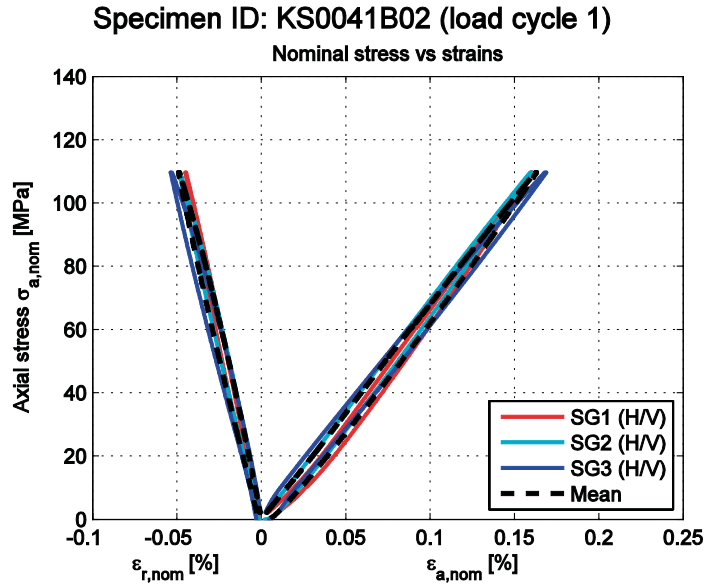

Figure 3-3. *Measured strains in the cylindrical part during the first load cycle on specimen KS0041B02 recorded by the three circumferentially (H) and the three axially (V) oriented strain gauges. The thick dashed lines display the mean values of the three gauges in respective orientation.*

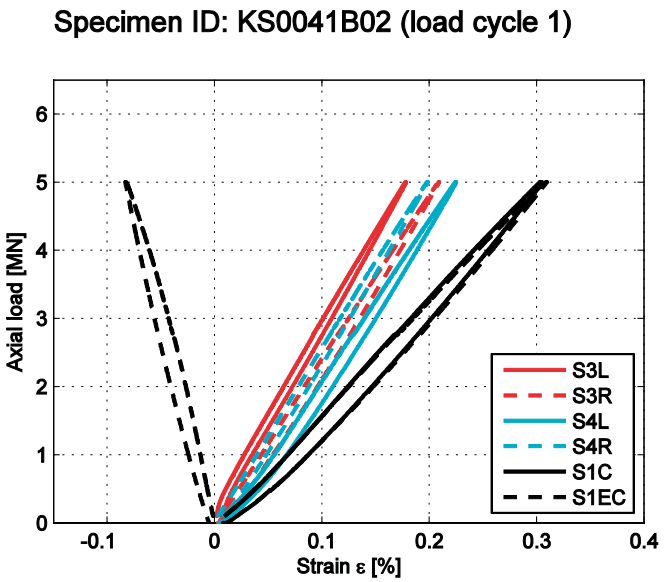

Figure 3-4. *Measured strains in the notch area during the first load cycle on specimen KS0041B02 recorded by the four strain gauges right outside the notch (black and red) and the two strain gauges placed in the centre of the notch (S1C) and the two directional strain gauge (S1EC) displaced 20 mm to the left of the centre.*

3.4 Acoustic emission

There was only one rather small AE-recording deviating a lot from the normal machine noise that was picked up during the test. The event took place at approximately 3.9 MN localized almost between AE sensor 3 and 4 (side 2), see Figure 3-5.

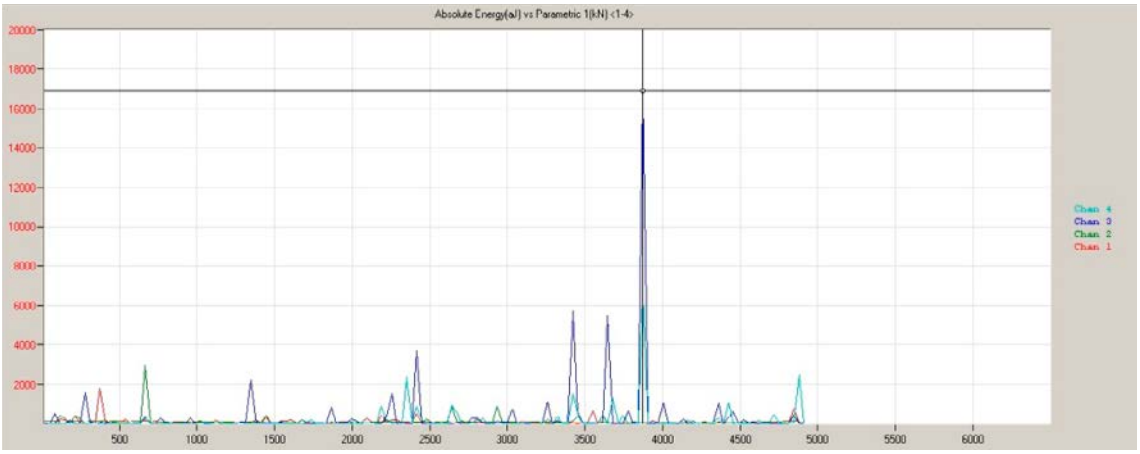

Figure 3-5. *Absolute energy for all four AE-sensors. A peak is shown at approximately 3.9 MN indicating crack initiation.*

4 Test of KS0041B02 (second load cycle, 0–6.4 MN)

4.1 Procedure

The specimen KS0041B01 was reloaded the next day after removing the electrical load cell. The force was from now on measured by means of recording the hydraulic pressure. The two notch areas of the specimen were covered over the night with a wet sponge cloth and sealed with plastics. It is not known how the moisture was preserved with this action. The sponge cloth was removed and water was sprayed on the notch areas prior to testing. The specimen was manually pre-loaded up to 0.5 MN. The initial loading rate was 0.20 MN/min up to 4.5 MN which was close to the previous maximum load that the specimen had experienced. The load rate was successively decreased in stages in order to be ready to act if large fracturing would occur. Moreover, it was of interest to notice at which load level the spalling would take place. Significant AE-activities were recorded at 6.38 MN whereby the test was aborted and the specimen was manually unloaded. The actual load rates for the test are shown in Figure 4-1.

4.2 Total deformations

The axial force versus the total deformation measurements are shown in Figure 4-2. The curves from measurements are again showing a slightly wavy behaviour. The average value of the three linear displacement transducers at the maximum load was 1.088 mm. This can be compared with a computed value of 1.171–0.055 = 1.116 mm. The computed value is the value from the FE-simulation of the KS0044B02 specimen adjusted due to that the KS0041B02 specimen was somewhat shorter than the KS0044B02 specimen.

4.3 Nominal strains and strains in the notch

The nominal stress versus strain in the cylindrical top part of the specimen is shown Figure 4-3. Both the individual strain gauges and their mean values are shown. The values of the elasticity constants were E = 71.5 GPa and ν = 0.33. The constants were evaluated as the secant value between 80 MPa and 120 MPa. The maximum nominal stress during the test was 140.0 MPa.

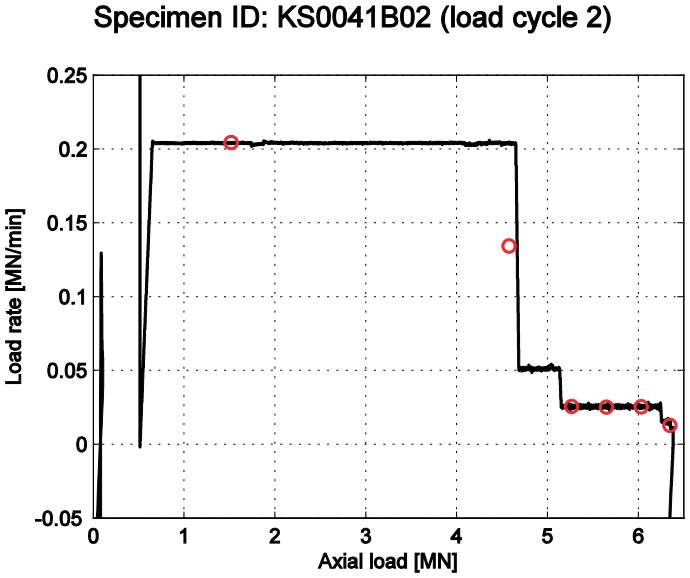

Figure 4-1. *The load history during the second load cycle on specimen KS0041B02. The red circles mark every 15 minutes test time. The oscillating behaviour is artificial and caused by the numerical computation of the load rate.*

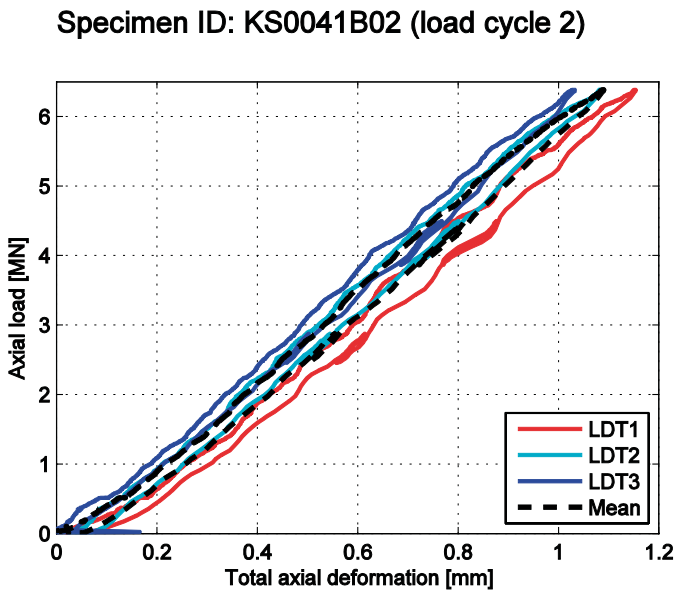

Figure 4-2. *Total axial deformation during the second load cycle on specimen KS0041B02 recorded by the three linear displacement transducers (LDT) and the mean value.*

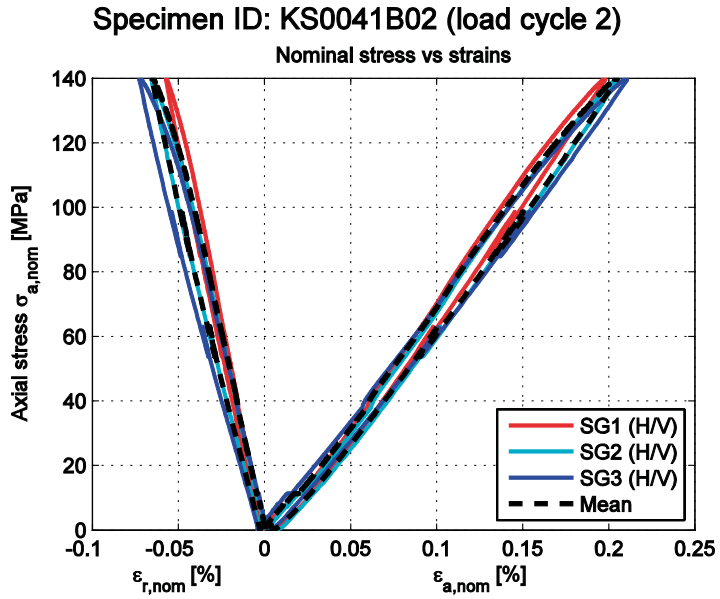

Figure 4-3. *Measured strains in the cylindrical part during the second load cycle on specimen KS0041B02 recorded by the three circumferentially (H) and the three axially (V) oriented strain gauges. The thick dashed line display the mean values of the three gauges in respective orientation.*

The recorded strains in the notch area are shown in Figure 4-4. Both strain gauges in the centre of the notch (S1C and S1EC) picked-up a small disturbance at 6.21 MN (231 MPa) and the one-sided strain gauge (S1C) lost the attachment completely at 6.29 MN (234 MPa). The stress values in the parentheses are estimated using the FE-simulations for the KS00044B02 specimen and are approximately one percent too high.

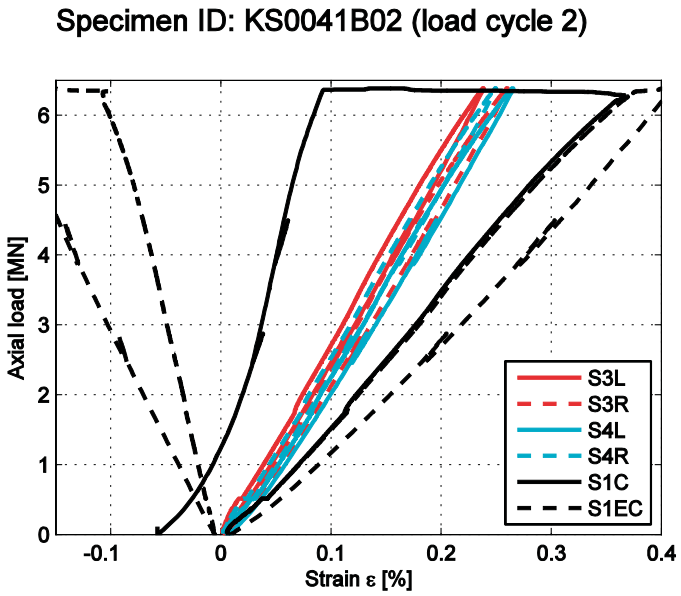

Figure 4-4. *Measured strains in the notch area during the second load cycle on specimen KS0041B02 recorded by the four strain gauges right outside the notch (black and red) and the two strain gauged placed in the centre of the notch (S1C) and the two directional strain gauge (S1EC) displaced 20 mm to the left of the centre.*

4.4 Acoustic emission

The test was performed continuously to about 6.4 MN (in AE system 6.25 MN due to a calibration bias). No AE recordings were recorded up to the previous load level in accordance with the expected Kaiser effect, cf. Lavrov (2003). Only the pump noise from a help device was recorded which could be confirmed by listening when the pump switched on and off. Signals from fracturing processes below the pump noise of 50 dB could therefore not be observed. This pump was not on during the first load cycle. No further analysis is done of signals below 50 dB.

The amplitudes of the AE-signals increased with higher load starting from about 5.3 MN (197 MPa), which is an indication of accelerated material degradation. First increase in AE intensity happened at around 5.7 MN (212 MPa) which caused a peak in the absolute energy measurements, see Figure 4-5 and 4-6. The first event exceeding 70 dB was exactly between sensor 1 and 2 on side 1 at 5.85 MN, see Figure 4-7. The first event exceeding 70 dB on side 2 (in the centre of the notch) occurred at 5.92 MN (220 MPa). The intensity in the energy accelerated until test was stopped at around 6.4 MN.

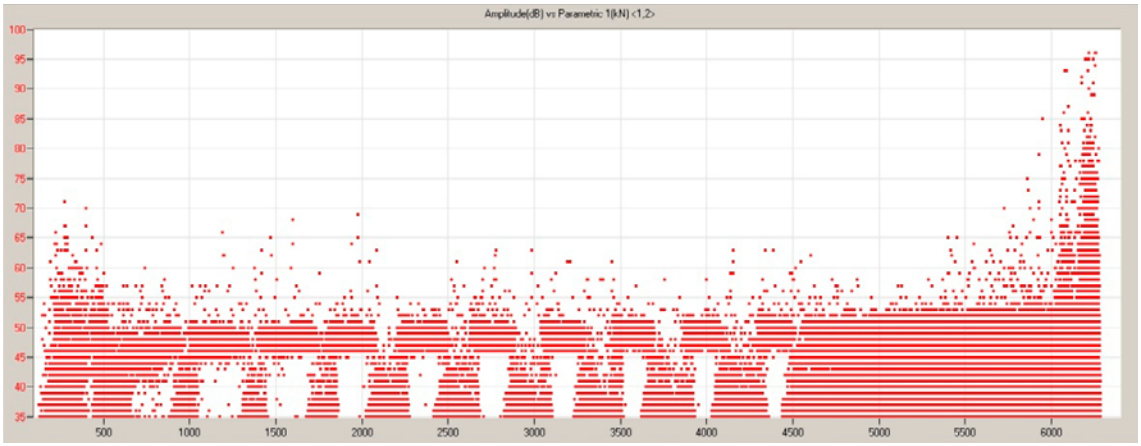

Figure 4-5. *Amplitudes for hits versus load for the complete test. Pump noise (periodical) on around 45–50 dB is shown. The successive increase of amplitudes and intensity starts at 5.3 MN which continues to increase until the test is stopped.*

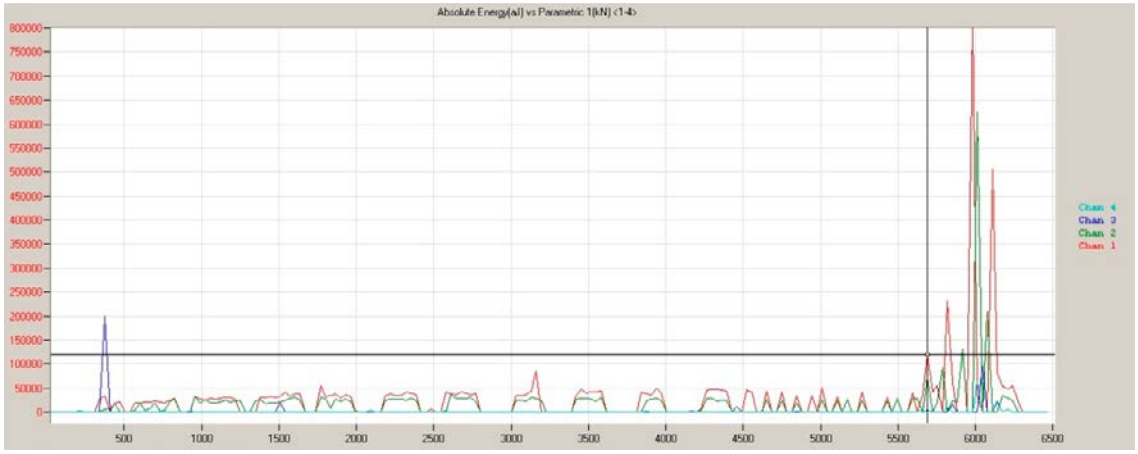

Figure 4-6. *Absolute energy for all four AE-sensors. A first significant peak is observed at 5.7 MN.*

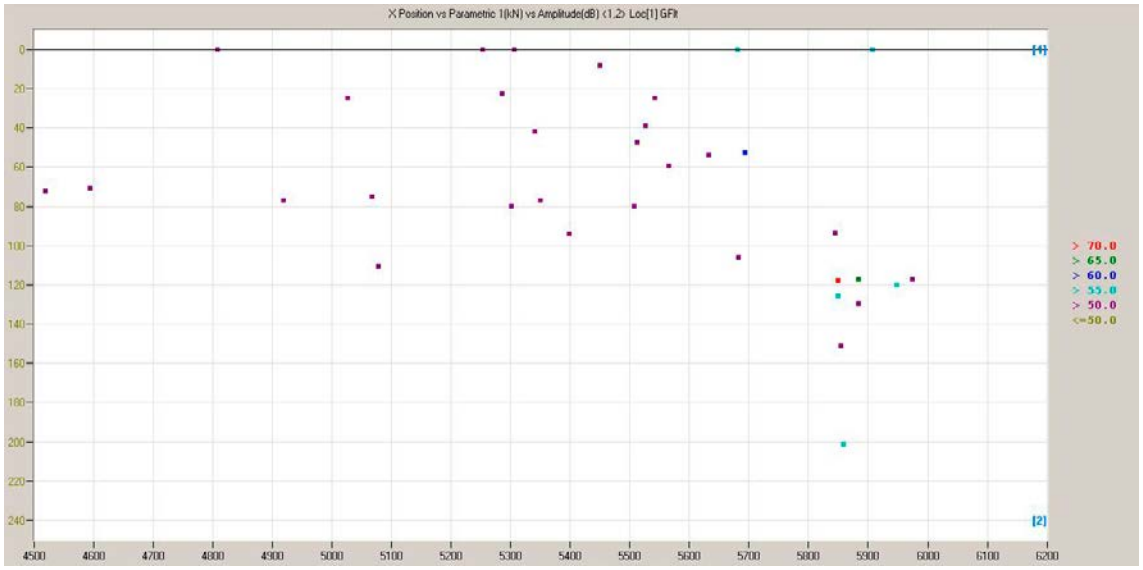

Figure 4-7. *The relative energy of the events in dB versus force. The first reading exceeding 70 dB (red marking) was at 5.85 MN localized exactly between sensor 1 and 2 on side 1.*

A localization analysis of the events in the plane between sensor 1 and 2 on one side and sensor 3 and 4 on the other side was done, see Figure 4-8. Three areas with clusters of signals were observed. Cluster 1 was inside the specimen but located closer to sensor 3 and 4 on side 2. Cluster 2 was also located inside the specimen, but closer to the surface but on the other side (side 1 between sensor 1 and 2). The third cluster was located on the surface on side 1 between sensor 1 and 2.

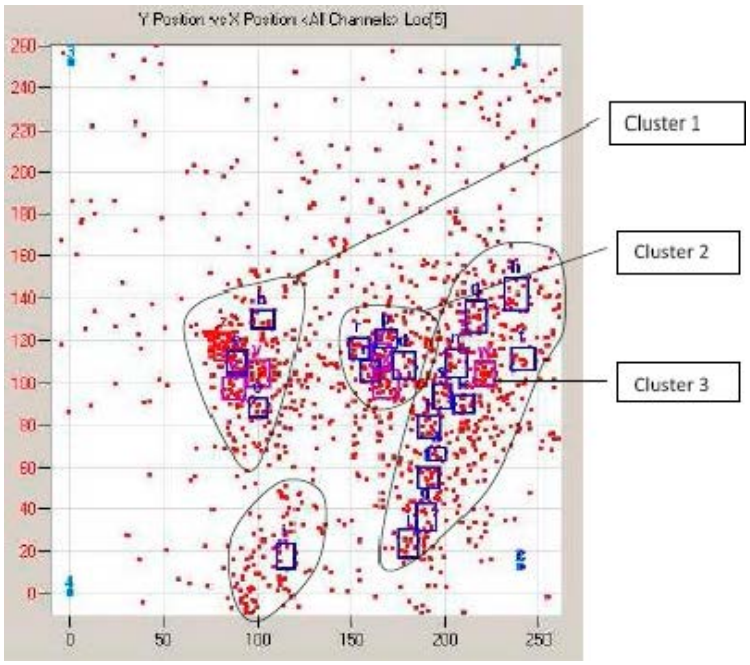

Figure 4-8. *2D-graph showing the area spanned by the four sensors (1 upper right, 2 lower right, 3 upper left, 4 lower left). The clusters show the locations of the events.*

4.5 Visual inspection of the spalling area

Some surface cracks are seen in the centre of the notch on side 1, cf. Figure 4-9. The rock surface is partly covered by the adhesive used for the strain gauges, which may have prevented some fracture propagation. No clear cracks were visible on side 2.

A post-characterization study of the fractures by means of microscopy were conducted, see Chapter 6. A slab was cut out from the specimen in the axial direction from notch to notch with an offset of 5 mm from the centre. The fracture pattern was examined using combined fluorescent and polarized microscopy. Thin sections were also taken from the specimen at both notches. A more detailed description of the investigation and the results is found in Chapter 6.

Figure 4-9. *Centre of the notch at side 1 of specimen KS0041B02 after testing. Some cracks are visible.*

5 Test of KS0044B02

5.1 Procedure

The specimen was kept moisture during the test by wetting a sponge cloth and lightly applying it against the notch surface. A piece of soft cell plastic was put outside the cloth to hold it in place. The arrangement is seen in Figure 2-6.

The specimen was manually pre-loaded up to 0.1 MN in order to settle all contacts. The initial loading rate from 0.1 MN was 0.2 MN/min up to 4.2 MN. The load rate was decreased in steps as the load level was approaching the level at which spalling was assumed to take place.

Significant AE-activities were recorded at 5.35 MN whereby the test was aborted and the specimen was manually unloaded. The actual load rates for the test are shown in Figure 5-1.

5.2 Total deformations

The axial force versus the total deformation measurements are shown in Figure 5-2. The curves from measurements are again showing a slightly wavy response. The average value of the three linear displacement transducers at the maximum load was 0.956 mm. This can be compared with a computed value of 0.917 mm.

5.3 Nominal strains and strains in the notch

The nominal stress versus strain in the cylindrical top part of the specimen is shown Figure 5-3. Both the individual strain gauges and their mean values are shown. The values of the elasticity constants were E = 61.0 GPa and ν = 0.36 evaluated as the tangent values between a nominal axial stress of 85–115 MPa and E = 64.2 GPa and ν = 0.29 evaluated as the secant values from 0.5–117.4 MPa. The maximum nominal stress during the test was 117.4 MPa.

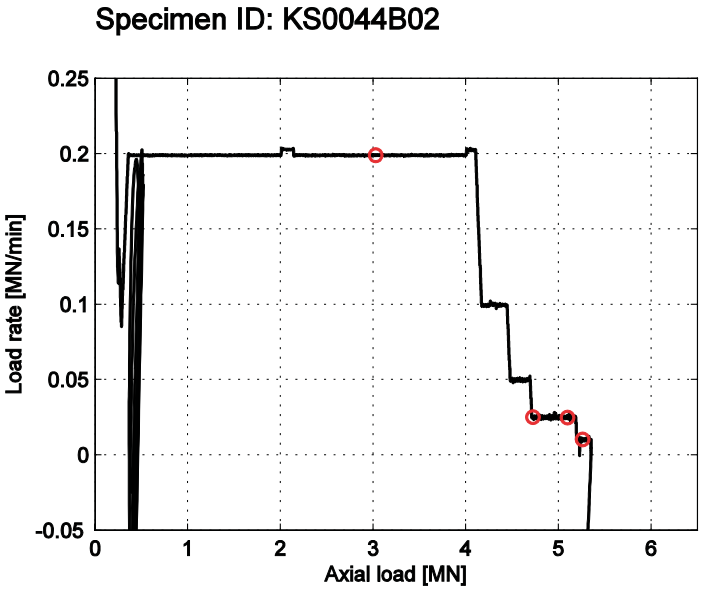

Figure 5-1. *The load history during the first load cycle on specimen KS0044B02. The red circles mark every 15 minutes test time.*

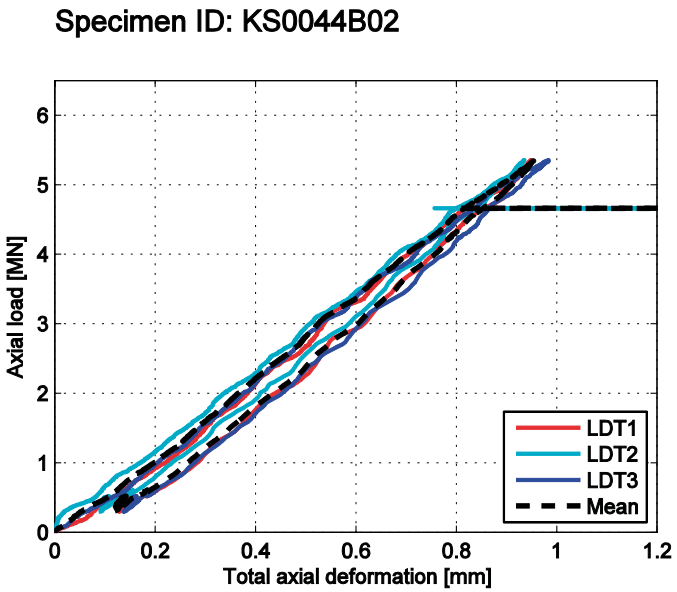

Figure 5-2. *Total axial deformation during the test on specimen KS0044B02 recorded by the three linear displacement transducers (LDT) and their mean value.*

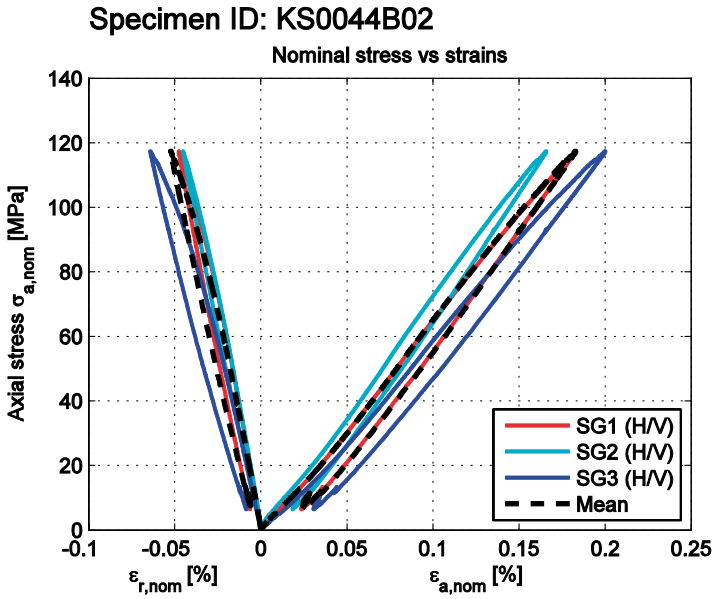

Figure 5-3. *Measured strains in the cylindrical part during the test on specimen KS0044B02 recorded by the three circumferentially (H) and the three axially (V) oriented strain gauges. The thick dashed line display the mean values of the three gauges in respective orientation.*

The recorded strains in the notch area are shown in Figure 5-4. Both strain gauges in the centre of the notch (S1C and S1EC) picked-up a small disturbance at 5.18 MN (193 MPa) and at 5.23 MN (195 MPa). The stress values in the parentheses are estimated using the FE-simulations.

An overall comparison of the strain measurements has been executed. The measured and computed strains obtained at 3.0 and 5.0 MN have been extracted and are shown in Table 5-1.

The values measured and computed strains match each other within a few percents relative difference. Some notable exceptions are from the circumferential strain measurements where the measured circumferential expansion is 34–45 % (3.0 MN) respective 13–32 % (5.0 MN) less than the computed strains. This may be related to end friction effect from the upper platen. The distance from the location of the strain measurement (90 mm below the platen) was too small.

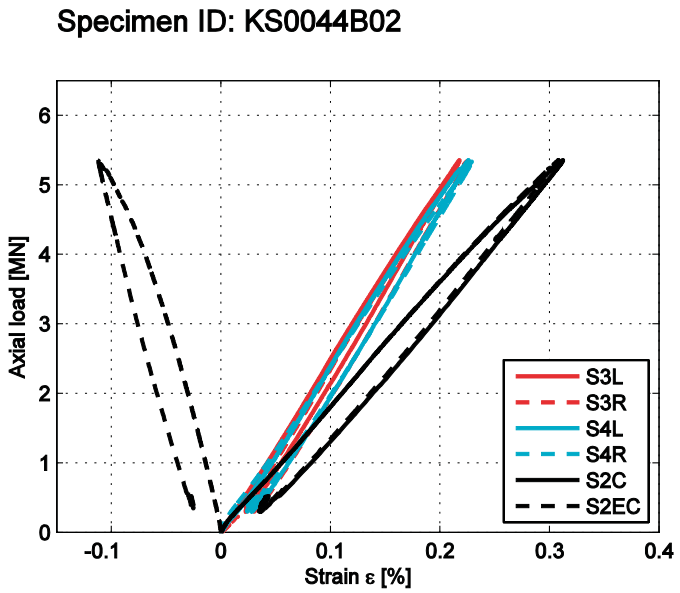

Figure 5-4. *Measured strains in the notch area during the test on specimen KS0044B02 recorded by the four strain gauges right outside the notch (black and red) and the two strain gauged placed in the centre of the notch (S2C) and the two directional strain gauge (S2EC) displaced 20 mm to the left of the centre.*

Table 5-1. Strains from computations, at the strain gauges and the relative difference at 3.0 and 5.0 MN.

	Strains (%) at 3.0 MN			Strains (%) at 5.0 MN		
Strain gauge	**Computed**	**Measured**	**Relative difference**	**Computed**	**Measured**	**Relative difference**
S1V	0.0975	0.102	4.6	0.162	0.171	4.7
S1H	–0.0326	–0.0222	–47	–0.0543	–0.0429	–27
S2V	0.0960	0.0919	–4.5	0.160	0.153	–4.3
S2H	–0.0323	–0.0219	–47	–0.0538	–0.0409	–32
S3V	0.105	0.112	6.0	0.176	0.185	5.2
S3H	–0.0387	–0.0288	–34	–0.0644	–0.0568	–13
S3L	0.124	0.120	–3.3	0.206	0.202	–1.8
S3R	0.123	0.125	1.1	0.205	0.207	0.81
S4L	0.123	0.124	0.32	0.205	0.208	1.0
S4R	0.124	0.125	1.3	0.206	0.214	3.5
S2CV	0.164	0.165	0.52	0.274	0.287	4.7
S2ECV	0.162	0.165	1.5	0.271	0.285	4.9
S2ECH	–0.0504	–0.0482	–4.5	–0.0840	–0.0975	14

5.4 Acoustic emission

The emission starts just above 3.0 MN at a position about 110 mm under sensor 3 (side 1). This corresponds to a stress of 112 MPa. Localized events between sensor 1 and 2 (side 2) respective sensor 3 and 4 (side 1) are shown in Figure 5-5. One observation is that there are much more recorded events by the 150 kHz-sensors (3 and 4) compared to the 60 kHz-sensors (1 and 2).

Next, we start by looking at the events localized between sensor 1 and 2 (side 2). There is a couple of readings with an amplitude exceeding 60 dB at 4.15 and 4.27 MN (154 and 159 MPa) which may be associated with crack initiation. Then there is an increase of amplitude at 4.6 MN (171 MPa) where the amplitude is above 70 dB. Finally, there is a significant increase of activities at 5.15 MN (192 MPa) with also high amplitudes related to severe cracking.

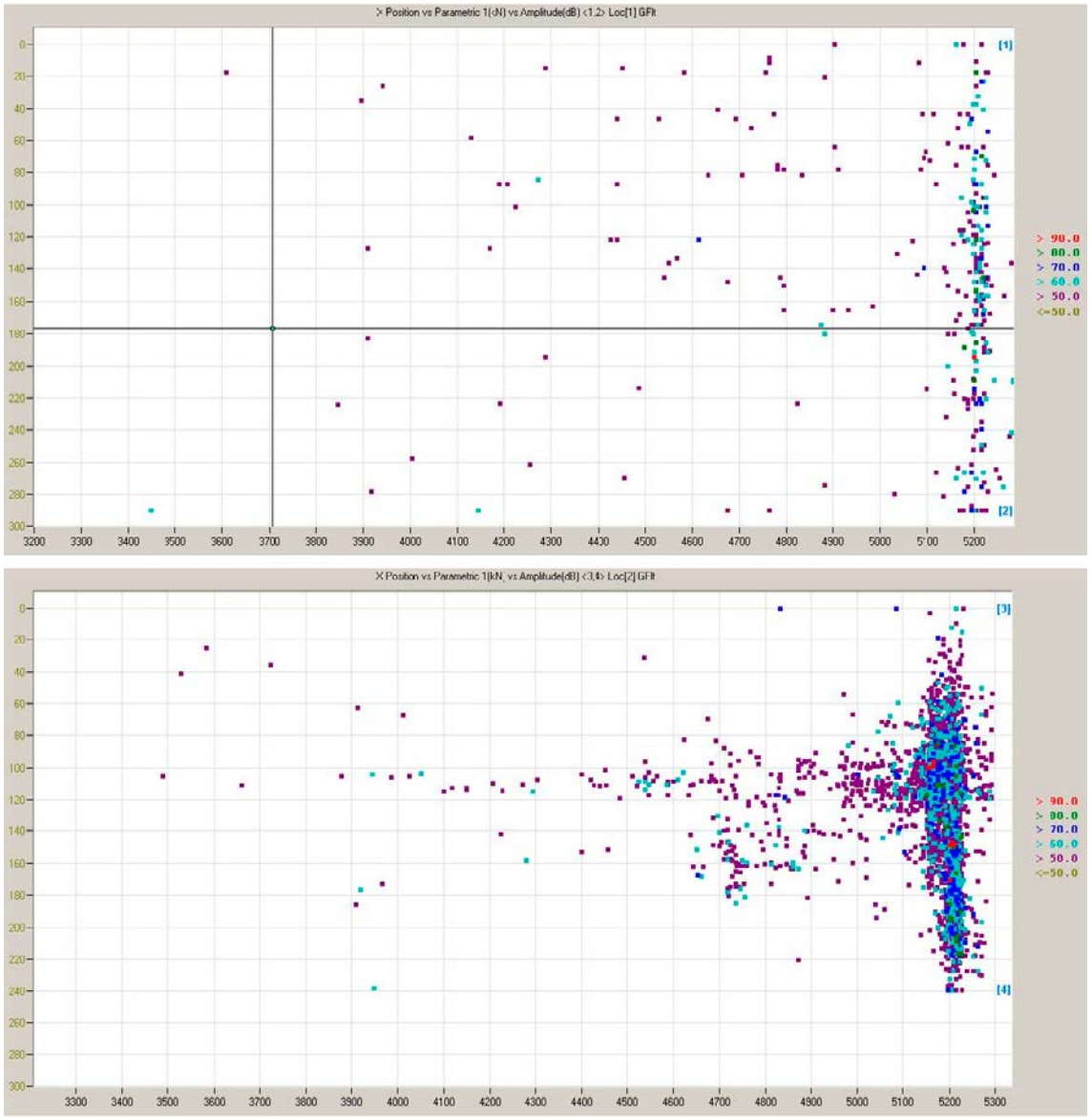

Figure 5-5. *Localization of events between sensors and their amplitudes versus force. Upper figure localization between 1 and 2 (side 2); Lower figure: localization between sensor 3 and 4 (side 1).*

As to the localisation of events between sensor 3 and 4 (side 1) there are some single recorded events with amplitude above 60 dB at 3.9 MN (145 MPa). This may be the onset of crack initiation. There is observed intensified activities at 4.5–4.6 MN (167–171 MPa) which could be regarded as the onset of systematic cracking. Severe cracking is taking place at 5.15 MN (192 MPa) which is associated with crack damage.

The number of the recorded events and amplitudes for senor 4 versus time is shown in Figure 5-6. There is a single strong event approximately 80 dB at 1 200 sec which corresponds to 4.0 MN (149 MPa). Moreover, there is a series of events right before 1 700 sec corresponding to 4.6 MN (171 MPa). There are severe activities with high amplitudes recorded at 2 850 sec and 3 100 sec (5.15 and 5.22 MN). These observations match well with Figure 5-6.

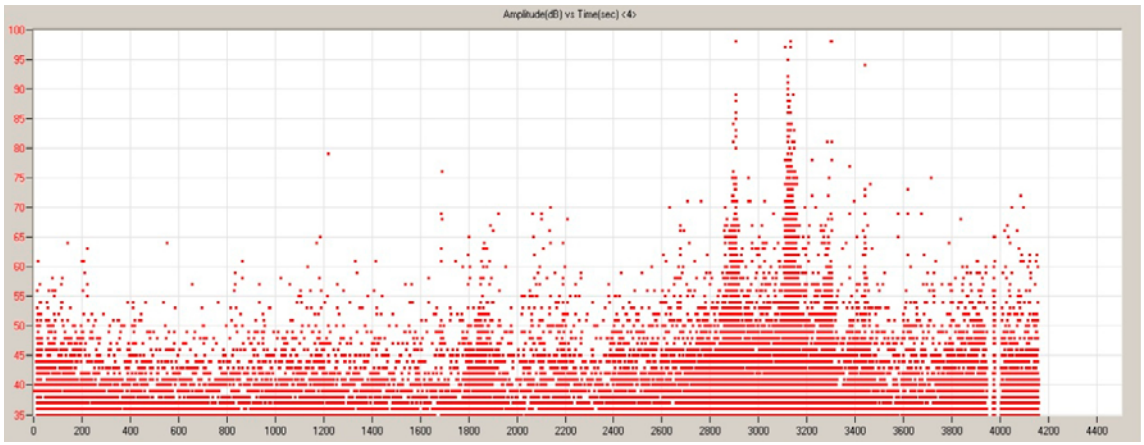

Figure 5-6. *Events recorded by sensor 4 and their amplitudes versus time.*

5.5 Visual inspection of the spalling area

Significant spalling can be seen on side 1 on specimen KS0044B02. The spalling area was about 85×45 mm, see Figure 5-7. Several fractures have been developed especially around the long mafitic xenolith. A first set of chips have formed and fallen off the specimen. Further development of chips can be seen. The chips can be seen in Figure 5-8.

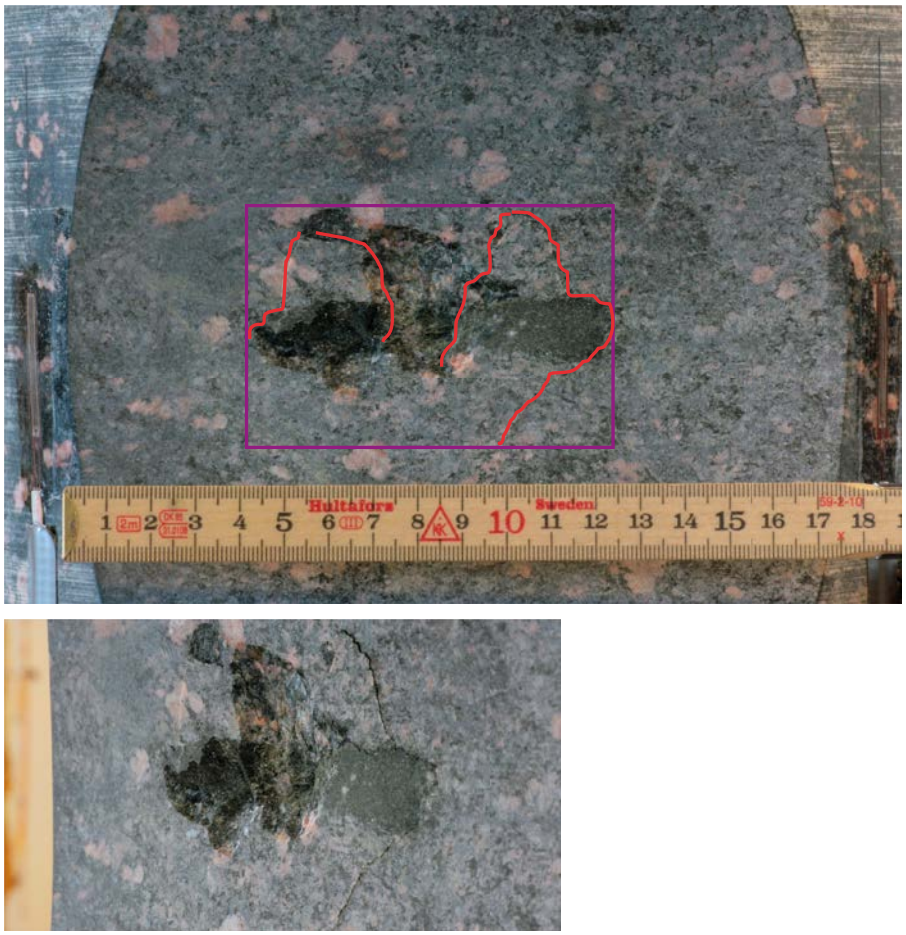

Figure 5-7. *Specimen KS0044B02 side 1. Spalling in the centre of the notch (85x45 mm) Upper picture: The red lines show the crack pattern of fully developed cracks; Lower picture: As above, but seen from the side. Chips of the rock material have fallen off the surface. Fractures around the long mafitic xenolith are visible.*

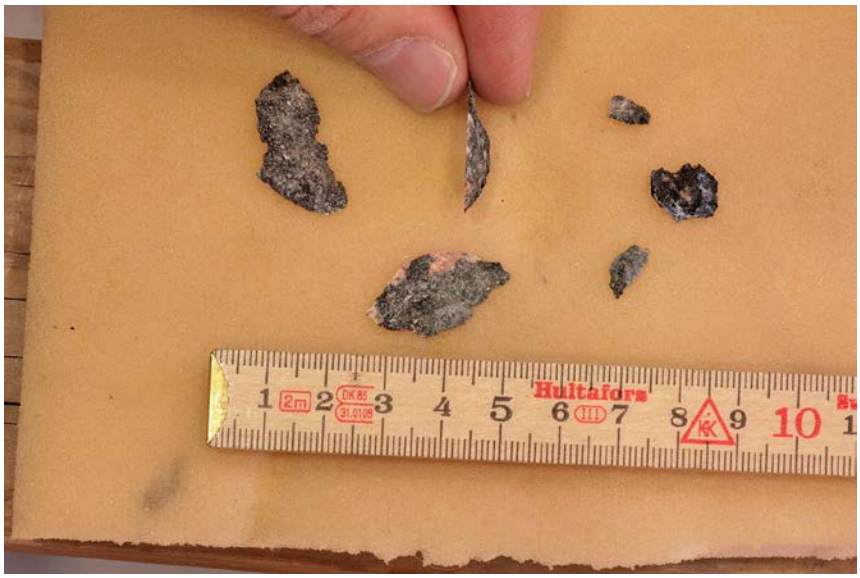

Figure 5-8. *Chips that has fallen off specimen KS0044B02. The pieces are up to 25–28 mm, thickness/ depth about 5 mm.*

The notch on side 2 of the specimen had strain gauges installed. No clear cracks were visible. The rock surface is partly covered by the adhesive used for the strain gauges, which may prevent fracture initiation.

A post-characterization study of the fractures by means of microscopy were conducted, see Section 6. A slab was cut out from the specimen in the axial direction from notch to notch with an offset of 5 mm from the centre. The fracture pattern was examined using combined fluorescent and polarized microscopy. Thin sections were also taken from the specimen at both notches. A more detailed description of the investigation and the results are found in Section 6.

6 Image analysis of combined fluorescent and polarized microscopic images

6.1 Descriptions of the specimens

The analyzed specimens are heterogeneous reddish grey, medium-grained, foliated quartz granitoids (so-called "Äspö diorite"). They contain plagioclase, quartz, K-feldspar, biotite, epidote, and accessory amphibole, sphene, chlorite, apatite and opaques. Large reddish K-feldspar megacrysts (1–3 cm) are characteristic for the rock. The K-feldspar megacrysts are generally parallel to the foliation, marked by red arrows in Figure 6-1. Mafic biotite-rich enclaves are abundant in the rock with the strike following the foliation of the rock.

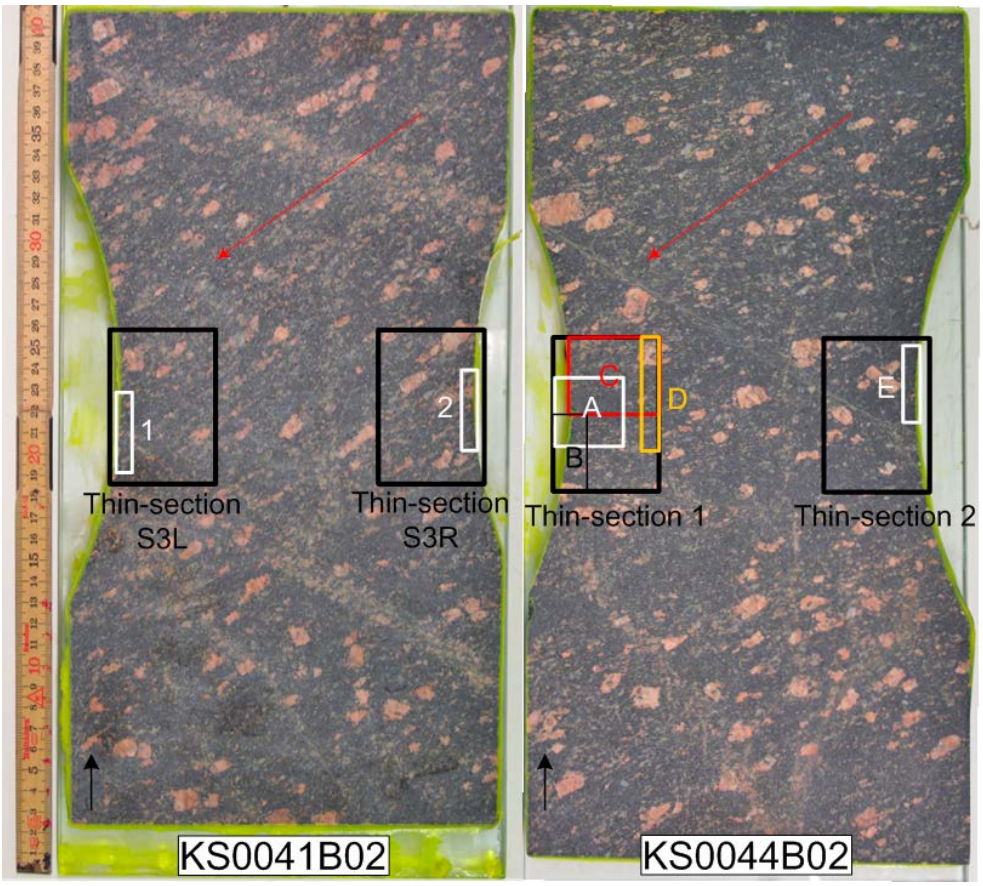

Figure 6-1. *Sawn plane polished slabs of specimen KS0041B02 and KS0044B02, impregnated with fluorescent epoxy. The analyzed planes are located c. 0.5 cm from the centre of the cylinder. Large black rectangles show the position of thin-sections, at the centre of the cylinder (different plane than the plane polished slabs). Smaller rectangles show the position of microphotographs of the thin-sections (Figures 6-2 to 6-8). Black arrows indicate way-up.*

6.2 Methods

The specimens were cut in half and plane polished slabs were prepared. These were impregnated with fluorescent epoxy. Thin-sections from respective overleaf of the slabs were also prepared and impregnated with fluorescent epoxy.

6.2.1 Macroscopic analyses

Cracks and fractures were studied and photographed in the plane polished slabs. Pictures were adapted in Photoshop Elements to increase the contrasts of the images.

6.2.2 Microscopic analyses

Thin-sections were photographed with optical microscopy for the image analyses of micro-cracks. The thin-sections were fixed on a motorized stage programmed so that images were photographed edge by edge, permitting a mosaic of images. The area for each image is 2.77×2.08 mm and the image resolution is 680×512 pixels. The same area was photographed with fluorescent light and polarized light. These images were later combined in Zeiss KS400 image processing system creating a combined mosaic of the fluorescent and polarized images. These images were used to determine crack initiation and propagation in the specimens.

6.3 KS0041B02

In sample KS0041B02, essentially no micro-cracks are visible in the combined polarized and fluorescent microscopic images of thin-section S3L (Figure 6-2). However, in the fluorescent images of both thin-sections of the sample, thin micro-cracks are visible around several quartz grains (cf. Figure 6-3). Biotite is occasionally also surrounded by thin, hardly visible micro-cracks. Feldspars generally lack grain boundary cracks, but sometimes hold intragranular cracks. In thin-section S3L very thin, up to 1 cm long intragranular cracks occur up to 2 cm from the notch.

In thin-section S3R one major fracture developed parallel to loading and the major principal stress field ($\sigma 1$), close to the perimeter of the notch (Figure 6-3). The $\sigma 1$-parallel cracks generally cut straight through quartz and feldspars, whereas when reaching biotite tend to follow their grain boundaries, causing a zig-zag-like pattern. Around the main fracture, several micro-cracks developed, also which are oriented parallel to $\sigma 1$. The main part of the cracks is located within or cross-cutting larger feldspar megacrysts. The cracks are also wider in the feldspars and tend to get thinner around the micas. Within the inner part of the thin-section feldspar host thin, hardly detectable, 0.25–0.5 cm long intragranular cracks and sparsely also micro-cracks crossing the feldspar boundaries, of which the longest is 1.5 cm (~1 cm from the notch). These cracks occur up to 4 cm from the notch in thin-section S3R.

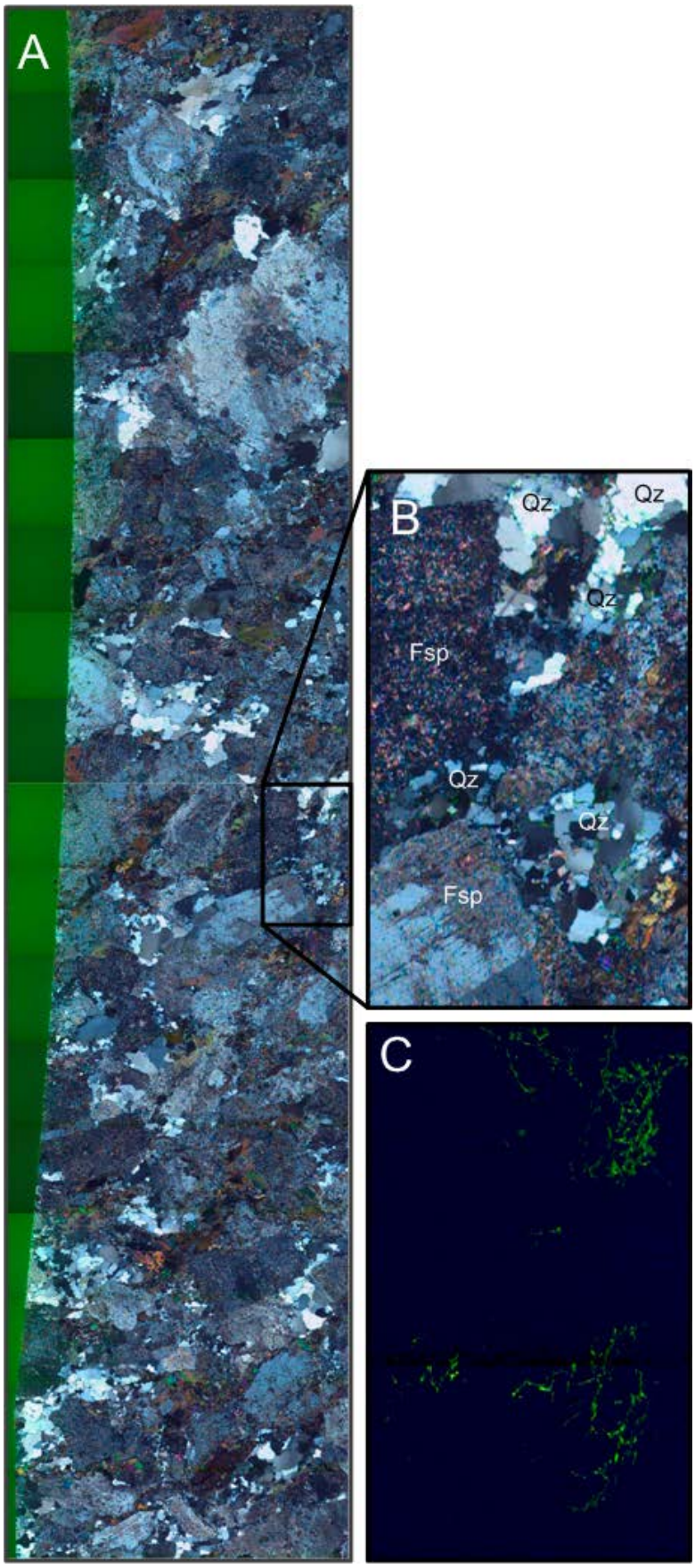

Figure 6-2. *A. Combined polarized and fluorescent microscopic image of KS0041B02 – Thin-section S3L – Image 1. Image size is 8.3 × 37.4 mm. B. Close-up of A. Fsp: feldspar, Qz: quartz C. Fluorescent microscopic image, same view as B.*

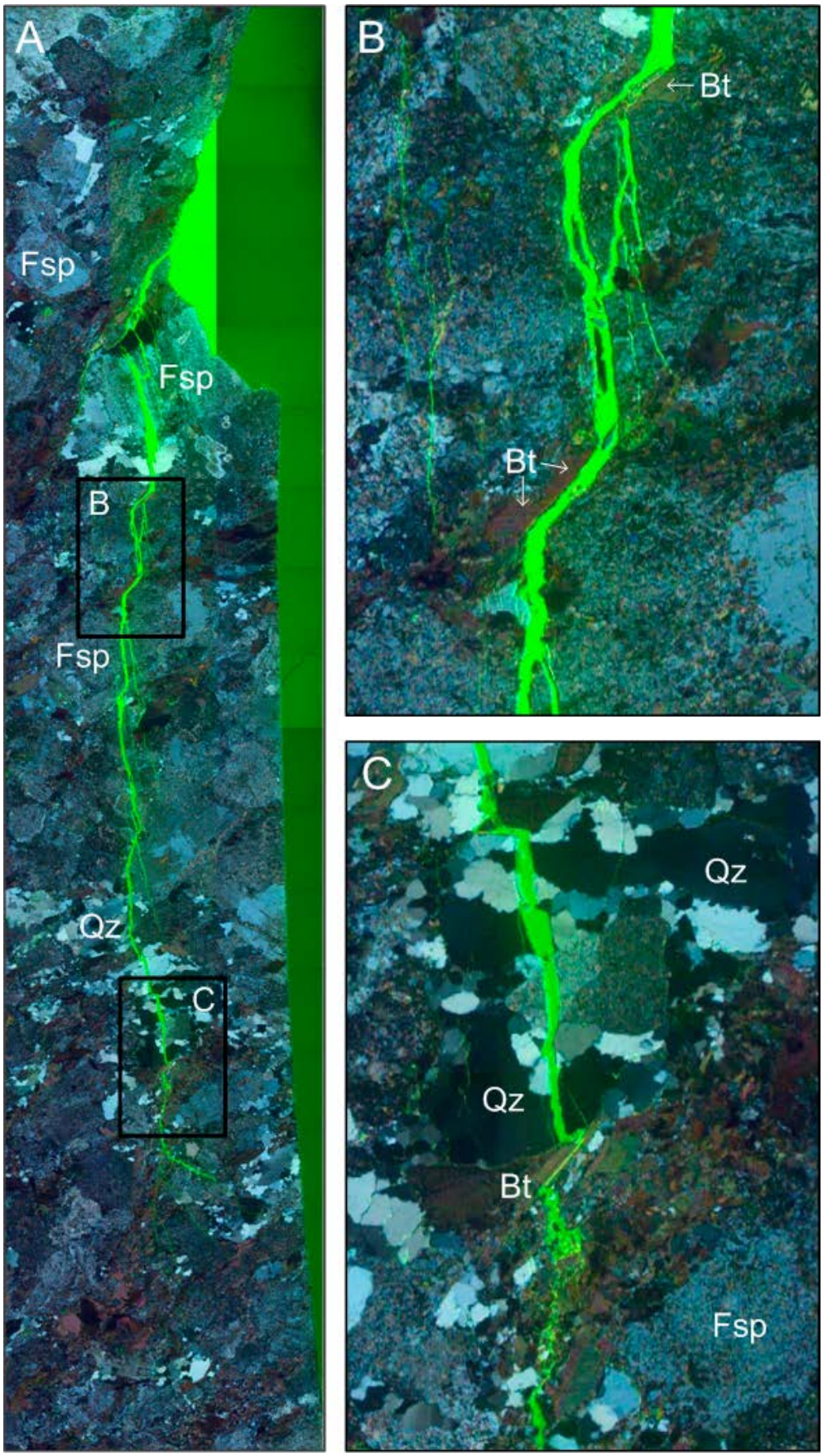

Figure 6-3. *A. Combined polarized and fluorescent microscopic image of specimen KS0041B02 – Thin-section S3R – Image 2. Image size of A is 8.3 × 37.4 mm. B and C are close up images of A. Bt: biotite, Fsp: feldspar, Qz: quartz.*

6.4 KS0044B02

Fractures in specimen KS0044B02 are more disturbed than in sample KS0041B02. Fracturing and spalling were generated where thin-section 1 is located and a large chip is missing in the thin-section (Figures 6-1 and 64 to 6-6). As seen in Figure 6-4, fractures are relatively heterogeneous, but the main orientation is parallel to loading and σ1, in connection to the perimeter of the notch. Micro-cracks also developed mainly parallel to σ1 (Figures 6-5 to 6-7).

Within the mafic enclave (darker area striking from the notch along the main foliation of the rock), two main cracks were developed. One of these cracks cross-cuts the foliation of the mafic enclave, approximately following σ_1, whereas the other crack is oriented roughly along the foliation of the mafic enclave. The cracks within the mafic enclave preferentially propagate towards the border of the enclave. The crack propagating inwards, along the foliation, generally propagates along grain boundaries of biotite within the enclave. The crack is subdivided near the boundary of the mafic enclave. One crack plunges upwards, through feldspars parallel to σ_1, whereas several smaller cracks are spreading and thinning inwards, towards the edge of the enclave, with one of these following the boundary before finally being obsolete. Smaller foliation-oriented micro-cracks are sparsely distributed within the mafic enclave (Figure 6-6).

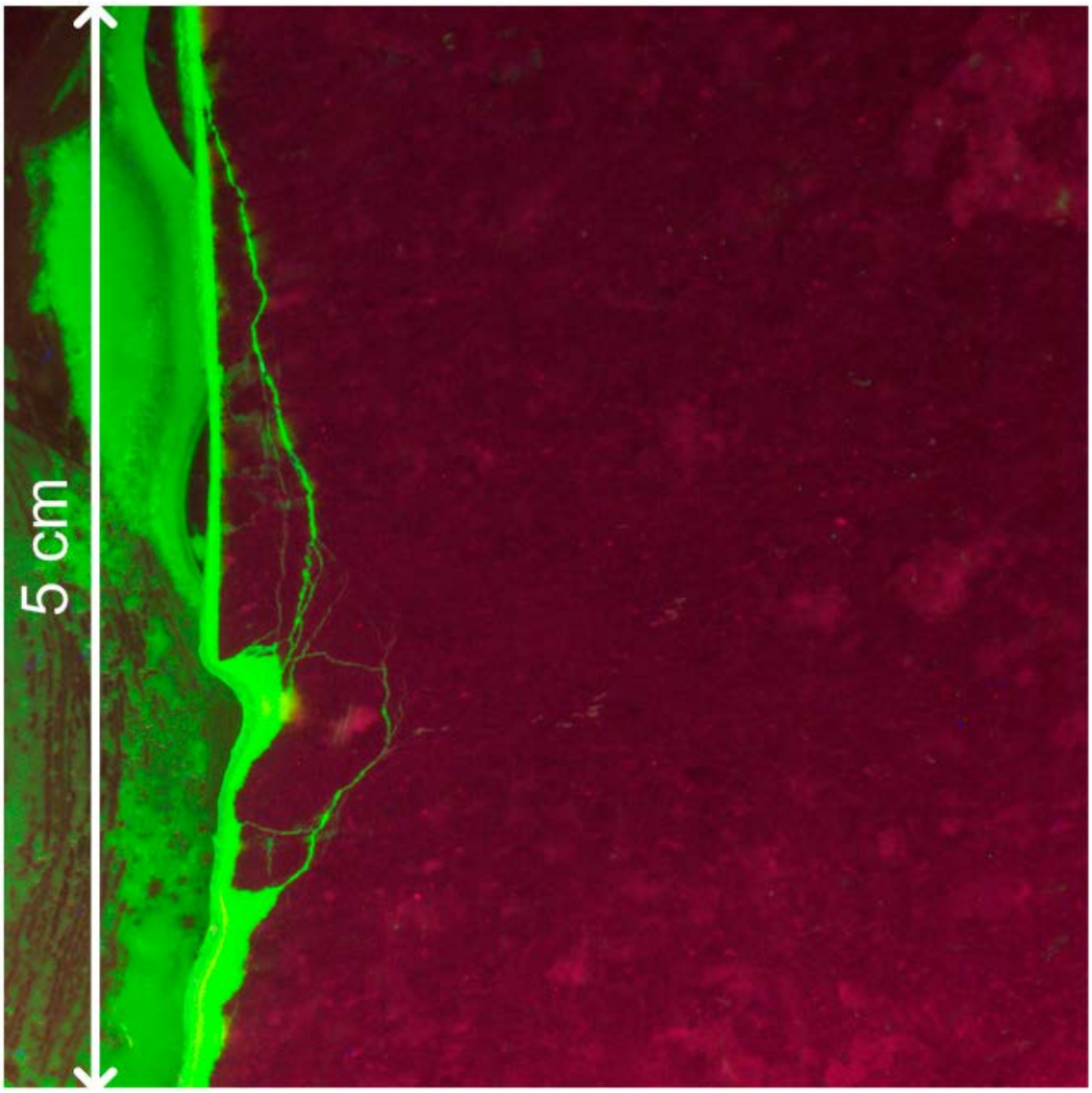

Figure 6-4. *Plane polished slab of specimen KS0044B02 – Image A, impregnated with fluorescent epoxy (close-up figure A of Figure 6-1). Image size is 5 × 5cm. The contrast and intensity of the image has been increased in Photoshop Elements.*

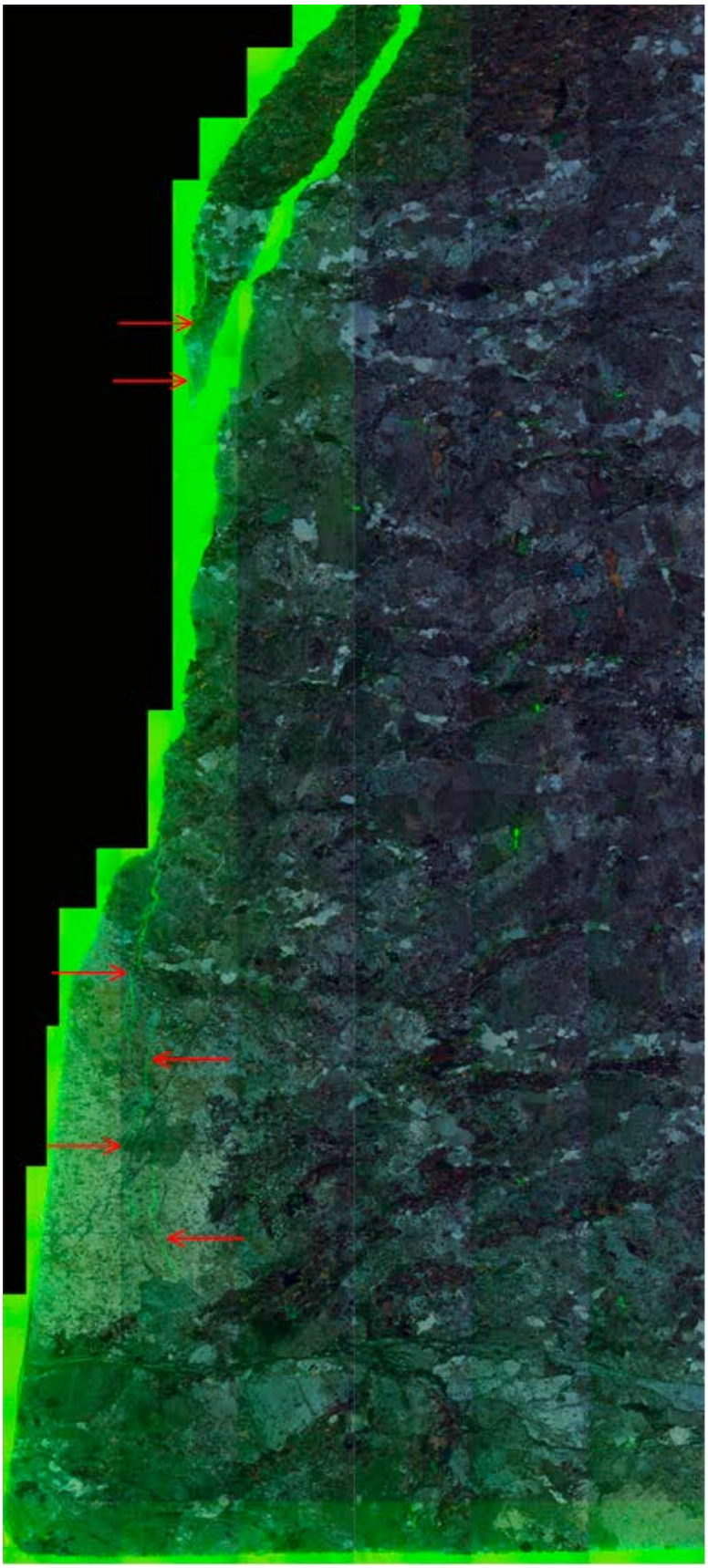

Figure 6-5. *Combined polarized and fluorescent microscopic image of specimen KS0044B02 – Thin-section 1 – Image B. Image size is 16.6 × 36.8 mm.*

The micro-crack plunging away from the mafic enclave (Figure 6-6), strike roughly parallel to σ1 and displays a similar pattern as cracks developed near the notch in Figure 6-5. These cracks generally cut straight through quartz and feldspars, whereas they follow the grain boundaries of biotite. The main part of the micro-cracks is located within or cross-cut larger K-feldspar megacrysts (cf. Figure 6-5). Intragranular micro-cracks occur up to 4 cm from the notch and are located within the feldspar megacrysts, the cracks oriented roughly parallel to σ1 (Figures 6-6 to 6-7).

Micro-cracks in thin-section 2 are preferentially located parallel to σ1 within feldspar megacrysts (Figure 6-8, red arrows pointing at micro-cracks). Longer micro-cracks (up to 1 cm) are exclusively located within the feldspar megacrysts. Some micro-cracks are also oriented perpendicular to σ1, within the feldspar megacrysts. Cracks are sparsely spread all over the thin-section, but are more common closer to the notch.

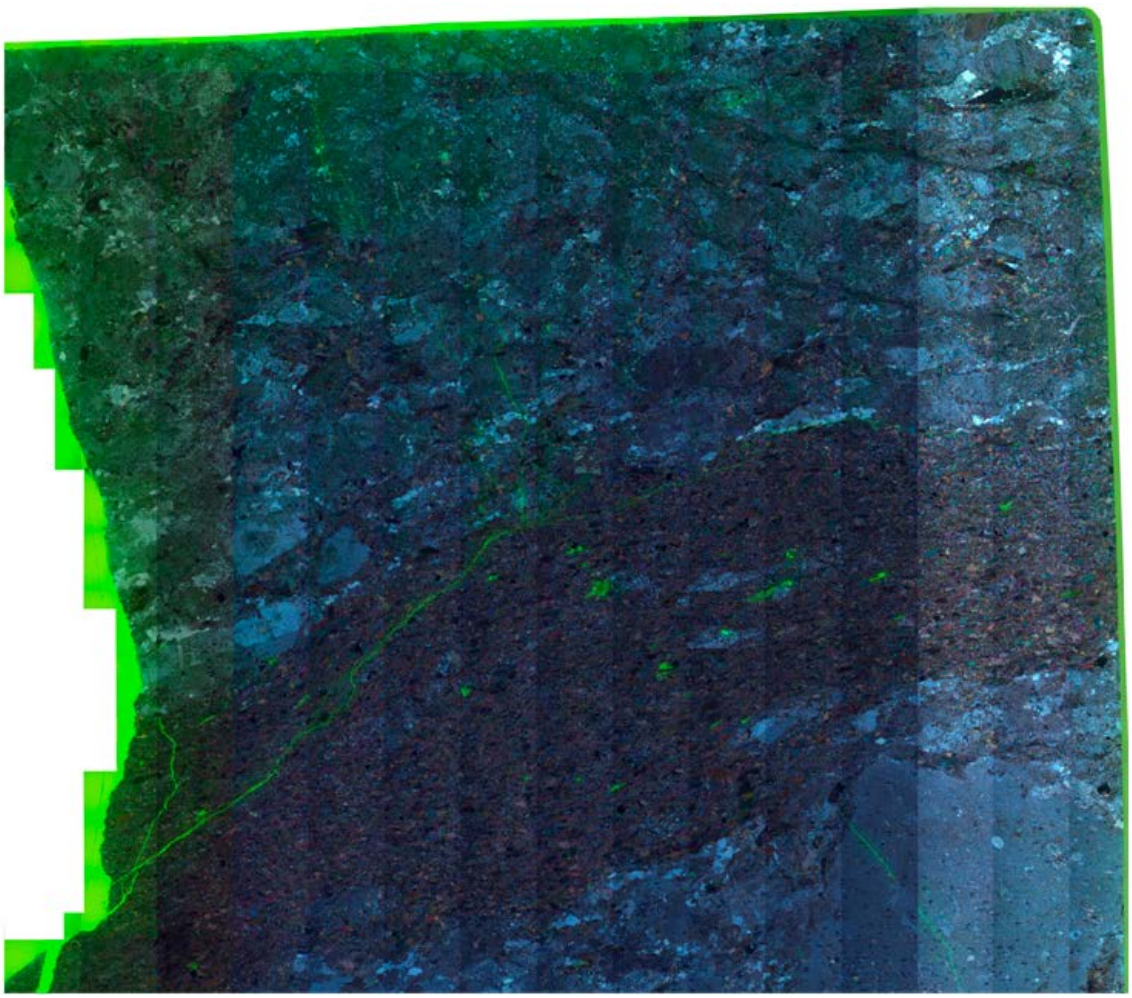

Figure 6-6. *Combined polarized and fluorescent microscopic image of specimen KS0044B02 – Thin-section 1 – Image C. Image size is 41.6 × 35.6 mm. Crack in the large K-feldspar megacryst, by the corner on the right-hand side, follows the joint in polarized image (somewhat darker line), although the fluorescent image showing the green crack is missing.*

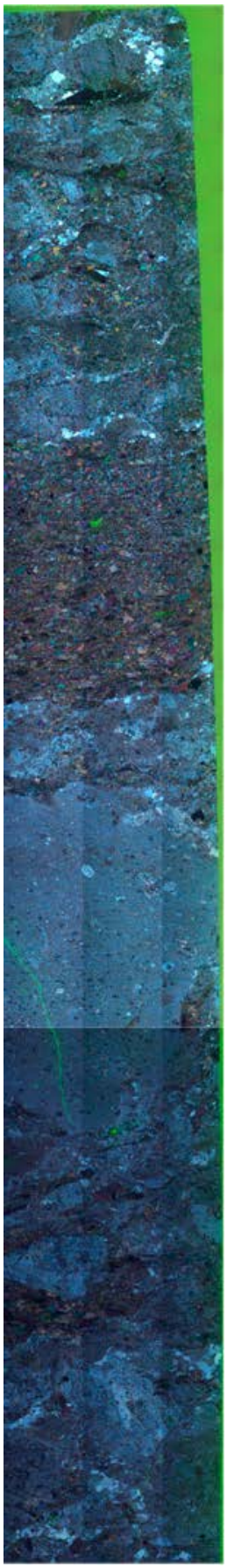

Figure 6-7. *Combined polarized and fluorescent microscopic image of specimen KS0044B02 – Thin-section 1 – Image D. Image size is 7.7 × 54.3 mm.*

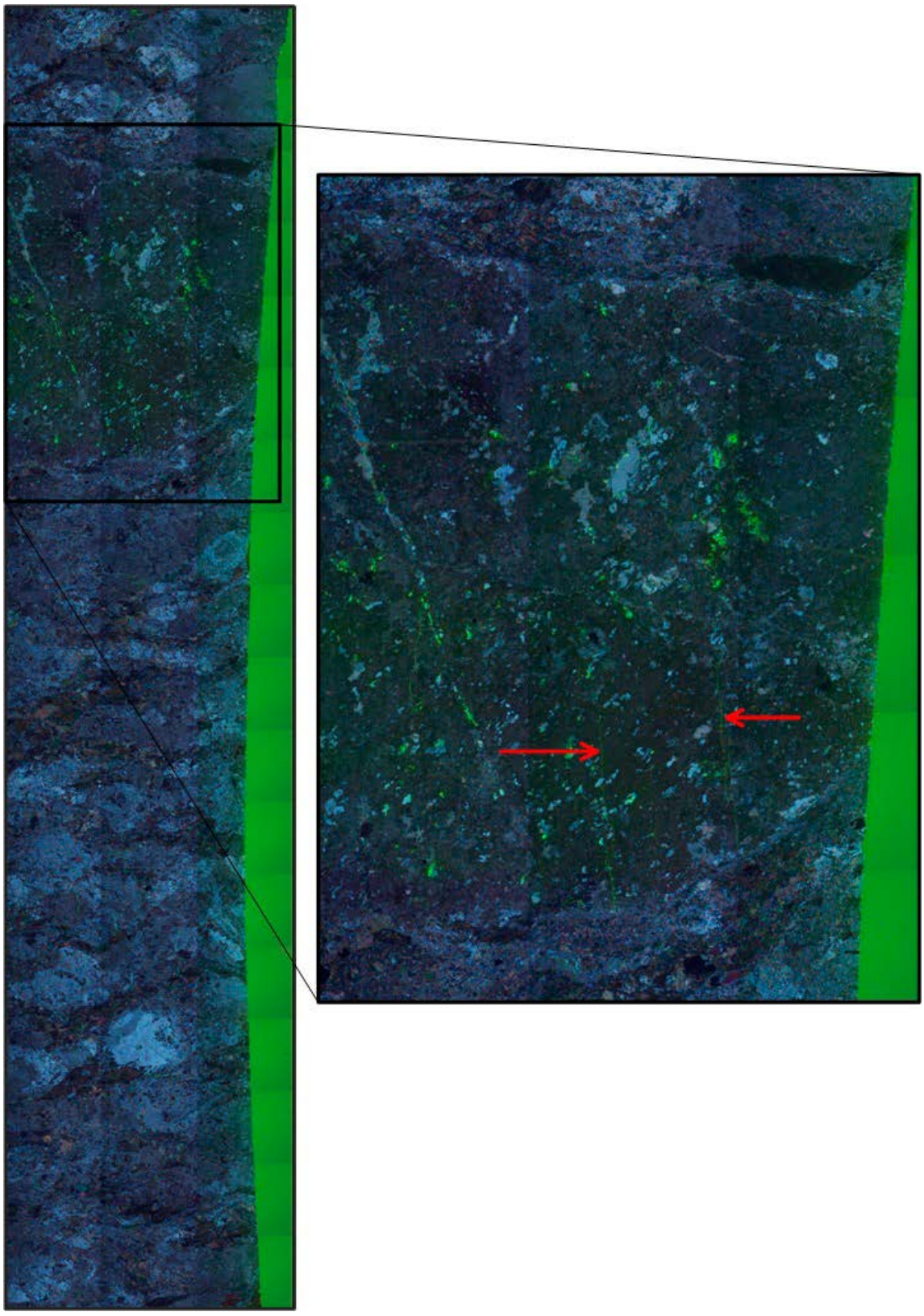

Figure 6-8. *Combined polarized and fluorescent microscopic image of specimen KS0044B02 – Thin-section 2 – Image E. Image size is 8.3 × 37.4 mm. Red arrows show intragranular cracks within altered feldspar.*

6.5 Discussion

Mechanical loading caused fracturing and spalling in both specimens, on one side each. Essentially all cracks are related to the "loading-induced" open fractures, although some micro-cracks were generated near one of the notches that did not develop spalling. The majority of the excavation fractures seem to be caused by extension along the major principal stress field ($\sigma 1$), although some shearing occurred as indicated by small displacements along the main excavation (cf Figure 6-9).

Micro-cracks are divided into intragranular- (within a mineral grain), transgranular- (crossing more than one grain) and grain boundary cracks. Grain boundary cracks within the matrix of the granitoids are more common in specimen KS0041B02 (cf. Figure 6-2), which merely reflects the abundance of quartz grains/aggregates. In contrast, specimen KS0044B02 lacks larger quarts-aggregates.

In general grain boundary cracks are not as common as intragranular and transgranular cracks and the grain boundary cracks are rarely coupled to transgranular cracks, fracturing and spalling. However, crack propagation sweep along biotite grain boundaries (as transgranular cracks) rather than through these grains and the properties of the mineral seem to control the behavior of the crack propagation in these grains.

Spalling-cracks in quartz-grains are almost solely transgranular and oriented parallel to $\sigma 1$, cutting straight through the mineral grains, regardless of the crystal lattice. Hence, the direction of the stress field controls the direction of the spalling-cracks in quartz.

Feldspar is more complex. The majority of the micro-cracks are intragranular or transgranular and oriented parallel to $\sigma 1$ (Figures 6-5 to 6-7). However, the direction of $\sigma 1$ roughly coincides with the crystal lattice of the feldspars. Hence it is impossible to say whether the cracks preferentially propagate through the crystal lattice or if they merely follow $\sigma 1$.

Most cracks developed in connection with the open spalling-fractures and propagate from them as transgranular cracks. However, large intragranular cracks are also found in the interior of the thin-sections, in K-feldspar megacrysts, suggesting that crack initiation may have started in these grains. Intragranular cracks are usually larger in "unaltered" feldspar megacrysts, where they propagate more easily. The lack of large "unaltered" K-feldspar megacrysts by the notches that did not develop spalling may also explain why spalling was favored on one side of each specimen. Specimen KS0044B02, with the more complex crack propagation further includes a mafic enclave. Hence, these heterogeneities probably act as critical disorders for the crack initiation.

As for biotite, in which the properties of the material seem to control the behavior of crack propagation rather than the stress field, the major crack in the mafic enclave preferentially propagates along its foliation, sweeping along the grain boundaries of biotite. The propagation also occurs close to the border of the mafic enclave, where less energy is required.

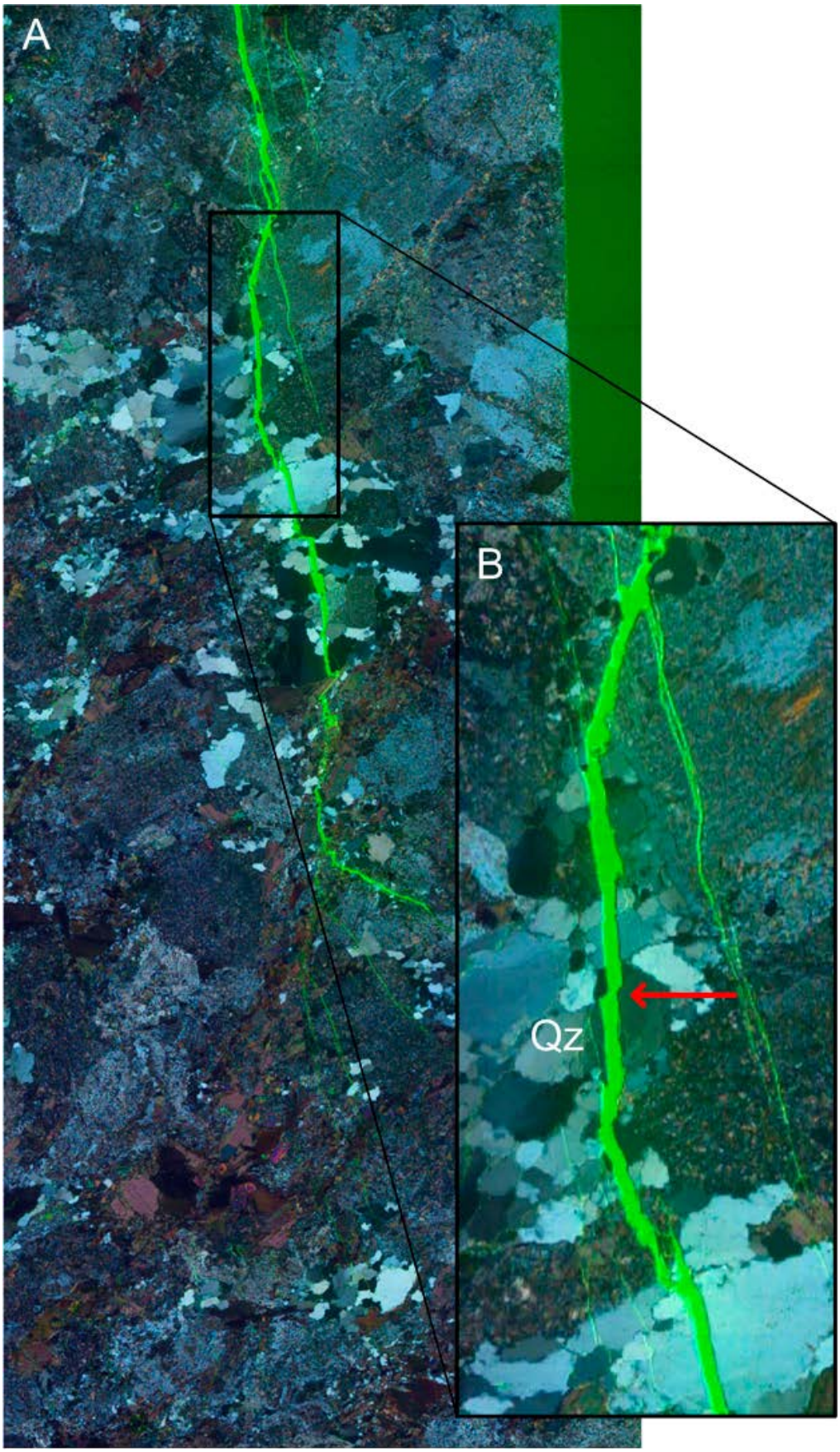

Figure 6-9. *Combined polarized and fluorescent microscopic image of specimen KS0041B02, where A is the lower half of Figure 3 (image size of A is 8.3 × 18.7 mm). Red arrow points at shearing displacement within quartz grain*

7 Summary and conclusions

The tests on the large cores showed that spalling could be localized to the notch areas as intended. The fractures and chips that were formed are similar to those found in the field.

The measured total deformation and strain correspond well with the predicted values from the FE-model of the specimen except for the circumferential strain at the cylindrical part of the specimen. The main role for the total deformation measurement was to provide an indication of possible bending of the specimen. The results of the strain measurements show that the results from the FE-model can be used to convert the measured load to stress values in the notch during the test, which is needed for the evaluation of the various stress thresholds of the fracturing stages.

There was a significant deviation between the measured and computed results of the nominal strains in the circumferential direction at the cylindrical part of the specimen. The reason for that could be a constraining of a radial expansion caused by the friction between the specimen and the loading platen. This can be confirmed by additional FE-simulations where the friction between the loading platen and the specimen is taken into account. One way to obtain better data of the nominal stress-strain relation is to create a more homogeneous deformation state by increasing the cylindrical part of the specimen.

The AE-measurements were essential in order to control when the test should be aborted as this was the only measurement by means of which it was possible to estimate the spalling initiation and progress in real time. The sensors with 150 kHz peak sensitivity provided more and better AE signals and were easier to use for source localization than the 60 kHz sensors. Both line and 2D-localization of the AE-signals seem to work well. The electrical load cell functioned as a mechanical filter isolating the pump noise during the first test. The pump noise was giving some disturbance during the last two tests after the electrical load cell was removed.

The various identified stress thresholds for the fracturing stages on the two specimens are summarized in Table 7-1. The stresses are entirely determined using results from the FE-model of the KS0044B02 specimen. The stress results for the KS0041B02 specimen in Table 7-1 are estimated to be approximately one percent to high due to a thicker waist between the notches. The fracture stages (crack initiation, coalescence and damage stresses) were identified using results from AE-measurements. The evaluation was rather subjective as it was the first time that this type of test was conducted. The results of the spalling initiation and coalescence stresses were higher than the values found from the uniaxial compression tests on the small cores, see Appendix A. It should be noted that the fracture process is slightly different between the notched specimens and the cylindrical cores and the results may not be fully comparable, cf. Figure 1-2. The ratio of the tangential stress over the compressive strength at initiation was about 0.71 for KS0041B02 and 0.98 for KS0044B02. This is significantly higher than from observations in field, cf. Andersson (2007) and Martin and Christiansson (2009).

Table 7-1. Different stress thresholds for the fracture stages for the two large specimens.

Specimen	Stage	Load (MN)	Stress (MPa)	Sensor	Side	Comment
KS0041B02	1 st act	3.95	147	3–4	2	Spalling chips on side 1
KS0041B02	Initiation	5.35	199	–	–	Specimen surface dried for 4 hours
KS0041B02	Coalescence	5.85	218	1–2	1	
KS0041B02	Damage	6.15	229	1–2	1	
KS0044B02	1 st act	3.00	112	3–4	1	Spalling chips on side 1
KS0044B02	Initiation	3.90	145	3–4	1	Surface kept wet during the test
KS0044B02	Coalescence	4.50	168	3–4	1	
KS0044B02	Damage	5.15	192	3–4	1	

All fracture stages were occurring at a much higher stress level for the KS0041B02 specimen. The difference was about 30 % compared with the KS0044B02 specimen, which could be explained by a number of reasons. Specimen KS0044B02 had a xenolith in the centre of the notch on side two where the spalling was occurring. The fractures are to some extent following the boundary between the xenolith and the neighbouring minerals. This may be the location and cause for a pre-mature failure and consequently one possibility for a lower stress for the fracture initiation.

Another difference between the two tests was the moisture condition. Specimen KS0041B02 was not moistured during the installation in the test device and not either during the actual test. The specimen surfaces were able to dry for approximately 4 hours. The notch surfaces on specimen KS0044B02 were moistured before the test and kept moistured by lightly attaching moistured sponge cloths to the notch surfaces.

Finally, the notches were carefully milled by successive tiny cuts and water cooling yielding a rather smooth surface which had been subjected to negligible heat exposure and forces during the machining. This yields a surface which has a minimum of initial damage that may result in an increased initiation stress as compared with drilled cores and at underground circular openings. This is in contrast with the large boreholes in the field which could have tougher loading history from the drilling operation. Finally, the size of the loaded volume is affecting the results. A larger highly stressed volume should lead to a lower initiation stress due to a larger probability that weak flaws are present. This is the case in situ.

The microscopy investigations of the specimens carried out after the testing are shown and summarised in Chapter 6. The investigations provide detailed information of the fracture process. The occurrence of microcracks and how they propagate through the different minerals and the location in relation to the notch, minerals and grain boundaries were investigated. The patterns of the major fractures and the secondary fractures were examined. The majority seem to be extension fractures, but shearing could also be verified. The results from the microscopy analysis provide invaluable information of the spalling process at all stages.

To conclude, we have shown results from compression tests with notched specimens resembling the geometry at a circular hole. The aim was to induce spalling as in an in situ condition along deposition boreholes and to determine the stress at which spalling is initiated. The failure process seems to be realistic judging from the rock chips that were formed. The double notch geometry, in this case, would approximately resemble a hole of 450 mm diameter which is much larger than the hole in the plate tests that were carried out by others, cf. Martin (1993). This makes the laboratory test with the double notched specimens unique in the perspective of simulation of large boreholes. However, the diameter of the planned deposition holes is about 1.8 m which is still much larger than the current tests, which means that there still remains a question about the effect of feedback confinement due to the curvature difference. Moreover, there is also still a question about the scale effects due to the size of the critical loaded volume (or area) on the results, although the scale difference is smaller than in several of the previously reported laboratory tests.

The current investigation provides new results for the understanding of the spalling problem. This is valuable since there is a need for a method to determine the crack initiation and damage stress in rock in a controlled repeatable way as an alternative to difficult in situ experiments such as those conducted by Martin (1993) and Andersson (2007).

The test needs to be further tuned regarding specimen geometry, moisture condition and surface properties in the notched areas as well as improving the analysis methods of the AE-results. Martin (1993) suggests that the crack initiation (σ_{ci}) and damage stress (σ_{cd}) are intrinsic parameters determining the long-term behaviour which should be used at dimensioning of underground facilities. Diederichs et al. (2004) mean that the crack coalescence stress (σ_{cs}) should be used instead of the crack damage stress to set the upper strength limit of the actual rock. Improved AE-measurements together with more comprehensive analysis of the acoustic events have to be considered in further development of the suggested test method. This would lead to better data and to a better understanding of the measurements such that a distinction of the various fracture stages according to Martin (1993) or Diederichs et al. (2004) can be carried out.

The microscopy analysis of the rock at the spalling area serves as a good complement to the other results as the fracture process within the grain structure at a meso-scale can be examined in detail.

Spalling fractures in the Äspö diorite are essentially developed parallel to loading, close to the perimeter of the notches and is caused by extension along the major principal stress field ($\sigma 1$). Some shearing must also have occurred as indicated by small displacements along the main excavation. Spalling-cracks are transgranular, cutting straight through most mineral grains, although they sweep along biotite grain boundaries. Intragranular micro-cracks within K-feldspar megacrysts occur sparsely throughout the thin-sections. The results indicate that the larger feldspar grains and mafic enclaves act as critical disorders for the crack initiation.

References

SKB's (Svensk Kärnbränslehantering AB) publications can be found at www.skb.com/publications.

Andersson J C, 2007. Rock mass response coupled to mechanical and thermal loading: Äspö pillar stability experiment, Sweden. PhD thesis. Royal Institute of Technology, Stockholm.

ASTM, 2001. ASTM D4543-01: Standard practice for preparing rock core specimens and determining dimensional and shape tolerance. West Conshohocken, PA: ASTM International.

Diederichs M S, Kaiser P K, Eberthardt E, 2004. Damage initiation and propagation in hard rock during tunneling and the influence of the near-face rotation. International Journal of Rock Mechanics and Mining Sciences 41, 785–812.

Eberhardt E, 1998. Brittle rock fracture and progressive damage in uniaxial compression. PhD thesis. University of Saskatchewan, Canada.

Edelbro C, 2008. Strength, fallouts and numerical modelling of hard rock masses. PhD thesis. Luleå University of Technology, Sweden.

Hakala M, Heikkilä E, 1997. Summary report – Development of laboratory tests and the stress-strain behaviour of Olkiluoto mica gneiss. Posiva 97-04, Posiva Oy, Finland.

ISRM, 1979a. Suggested method for determining the uniaxial compression strength and deformability of rock materials. International Journal of Rock Mechanics and Mining Sciences & Geomechanics Abstracts 16, 135–140.

ISRM, 1979b. Suggested method for determining water content, porosity, density, absorption and related properties and swelling and slake-durability index properties. International Journal of Rock Mechanics and Mining Sciences & Geomechanics Abstracts 16, 141–156.

Labuz J F, Dai S-T, Papamichos E, 1996. Plane-strain compression of rock-like materials. International Journal of Rock Mechanics and Mining Sciences & Geomechanics Abstracts 33, 573–584.

Lavrov A, 2003. The Kaiser effect in rocks: principles and stress estimation techniques. International Journal of Rock Mechanics and Mining Sciences 40, 151–171.

Martin C D, 1993. The strength of massive Lac du Bonnet granite around underground openings. PhD thesis. University of Manitoba, Canada.

Martin C D, Christiansson R, 2009. Estimating the potential for spalling around a deep nuclear waste repository in crystalline rock. International Journal of Rock Mechanics and Mining Sciences 46, 219–228.

Martin C D, Martino J B, and Dzik E J, 1994. Comparison of borehole breakouts from laboratory and field tests. In Proc. EUROCK'94, SPE/ISRM Rock Mechanics in Petroleum Engineering, Delft, pages 183–190, A.A. Balkema, Rotterdam.

SIS, 2002. SS-EN 13755: Natural stone test methods – Determination of water absorption at atmospheric pressure. Stockholm: Swedish Standards Institute.

Staub I, Andersson J C, Magnor B, 2004. Äspö Pillar Stability Experiment. Geology and mechanical properties of the rock in TASQ. SKB R-04-01, Svensk Kärnbränslehantering AB.

Appendix A

Uniaxial compression tests on small cores from KS0037B02

A.1 Specimens

Cores with a diameter of 50.8 mm were drilled out of the KS0037B02 core. Three specimens, which were free of visible weakness planes, were taken out of the drilled cores. The specimens were cut using a circular saw with a diamond blade and grinded in accordance with ASTM (2001) to fulfil the geometrical requirements. The specimens were labelled by SP, see Table A-1. The specimens were submerged into water and stored in water for 12–15 days until the time for the mechanical testing to obtain water saturated specimens in accordance with SIS (2002) reflecting in situ conditions. The wet density was measured when the specimen had been stored in water for 8 days according to ISRM (1979b). The expanded uncertainty with covering factor 2 (95 % confidence interval) is ± 4 kg/m^3 for determination of wet density.

Table A-1. Specimen identification, dimensions and rock type for all specimens.

Identification	Diameter (mm)	Height (mm)	Rock type/occurrence
KS0037B02-113-1	50.8	127.4	Äspö diorite
KS0037B02-113-2	50.8	127.3	Äspö diorite
KS0037B02-113-3	50.8	114.4	Äspö diorite

A.2 Execution

A.2.1 Test set-up

The mechanical tests were carried out in a servo controlled testing machine specially designed for rock tests, see Figure A-1. The axial load was measured using an electrical load cell with a maximum capacity of 1.5 MN. The uncertainty of the load measurement is less than 1 %. The uniaxial compression tests were carried out in accordance with ISRM (1979a) using stress control with a loading rate of 60 MPa per minute up to failure. The deformations were measured using six metal foil strain gauges. The gauge length should be many times larger than the grain size in the rock material in order to capture a homogenised response. Strain gauges with a gauge length of 20 mm were used which were mounted at mid height of the specimens, three in the axial and three in the circumferential direction, respectively. The strain gauges were placed with a 120 degrees division around the circumference labelled AV, BV and CV (axial direction) and AH, BH and CH (circumferential direction, see Figure A-2. The strain gauges were mounted on the specimens after 9, 12 and 13 days storage in water, respectively. The data acquisition was made with a HBM MGCplus unit. The tests were conducted starting with a pre load of 1 MPa and then a loading rate of 60 MPa/minute up to failure.

Acoustic emission measurements were carried out during the test of specimen KS0037B02-113-2 using equipment from Physical Acoustics Scandinavia. Two AE-sensors (60 and 150 kHz peak sensitivity) were attached to the lower loading platen using contact grease and tape, see Figure A-2. The test was aborted when the loading had reached 178 MPa and was unloaded in order to not damaging the AE-sensors in case of specimen failure. The AE-sensors were removed and the test was resumed, loading the specimen up to failure under the new identification KS0037B02-113-2x.

Figure A-1. *Rock testing system. From left: Digital controller unit, pressure cabinet (used for triaxial tests) and load frame. The PC with the test software (not shown in the picture) is placed on the left hand side of the controller unit.*

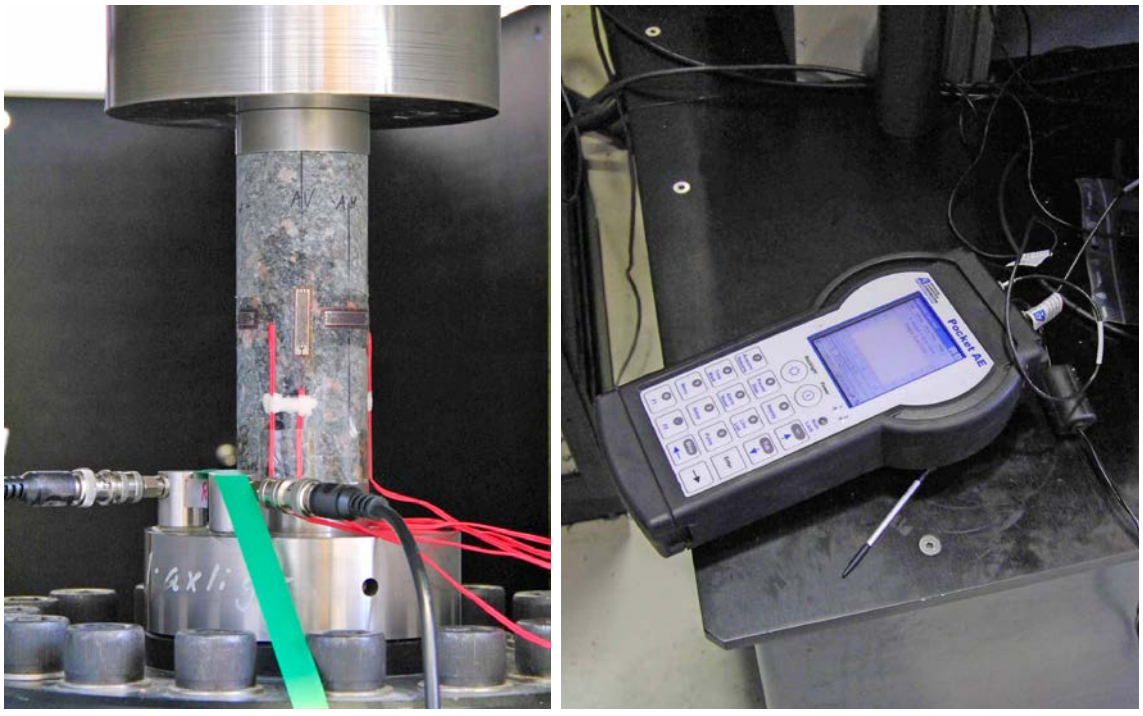

Figure A-2. *Left: Specimen with mounted strain gauges (CH, AV and AH are visible) and placed between the loading platens. AE-sensors are attached against the lower loading platen using contact grease and tape. Right: Pocket AE-device used during the AE-recordings.*

A.2.2 Analyses and interpretation

As to the definition of the different results parameters we begin with the axial stress σ_a, which is defined as

$$\sigma_a = \frac{F}{A} \qquad \text{Equation A-1}$$

where F is the axial force acting on the specimen, and A is the specimen cross section area. The peak value of the axial stress during a test is representing the uniaxial compressive strength σ_c in the results presentation. The axial strain ε_a is obtained as the mean value of the three axially mounted strain gauges AV, BV and CV, respectively. The radial strain ε_r is obtained as the mean value of the three circumferentially mounted strain gauges AH, BH and CH, respectively. The stresses and the strains are defined as positive in compressive loading and deformation. The elasticity parameters are defined by the tangent Young's modulus E and tangent Poisson's ratio ν as

$$E = \frac{\sigma_a(0.60\sigma_c) - \sigma_a(0.40\sigma_c)}{\varepsilon_a(0.60\sigma_c) - \varepsilon_a(0.40\sigma_c)}$$

$$\nu = -\frac{\varepsilon_r(0.60\sigma_c) - \varepsilon_r(0.40\sigma_c)}{\varepsilon_a(0.60\sigma_c) - \varepsilon_a(0.40\sigma_c)} \qquad \text{Equation A-2}$$

The tangents were evaluated with values corresponding to an axial load between 40 % and 60 % of the axial peak stress σ_c.

Results on volumetric strain and crack volume strain are reported. The volumetric strain ε_{vol} is defined as

$$\varepsilon_{vol} = \varepsilon_a + 2\varepsilon_r \qquad \text{Equation A-3}$$

By subtracting the elastic volumetric strain ε^e_{vol} from the total volumetric strain, a volumetric strain corresponding to the crack volume ε^{cr}_{vol} is obtained. This has been denoted calculated crack volumetric strain in the literature, cf. Martin (1993) and Eberhart (1998). We thus have

$$\varepsilon^{cr}_{vol} = \varepsilon_{vol} - \varepsilon^{e}_{vol} \qquad \text{Equation A-4}$$

Assuming linear elasticity leads to

$$\varepsilon^{cr}_{vol} = \varepsilon_{vol} - \frac{1 - 2\upsilon}{E}\sigma_a \qquad \text{Equation A-5}$$

where $\sigma_r = 0$ was used. The axial stresses on which the onset of an increased crack volume strain and total volumetric strain during uniaxial compression of intact rock core specimens without sealed joints occur, have commonly been related to the crack initiation stress σ_{ci} and the crack damage stress σ_{cd} respectively, cf. Martin (1993) and Eberhart (1998). The interpretation of the volumetric strains results versus axial stress is, however, unclear when the rock contains sealed joints.

A.3 Results

A.3.1 Individual specimens

Presentations of the individual specimens including results are shown in Figures A3 to A9.

Specimen ID: KS0037B02-113-1

Before mechanical test

After mechanical test

Diameter (mm)	Height (mm)	Density (kg/m^3)
50.8	127.4	2770
Comments:	–	

Figure A-3. *Specimen KS0037B02-113-1: Photographs before and after testing, dimensions and measured wet density.*

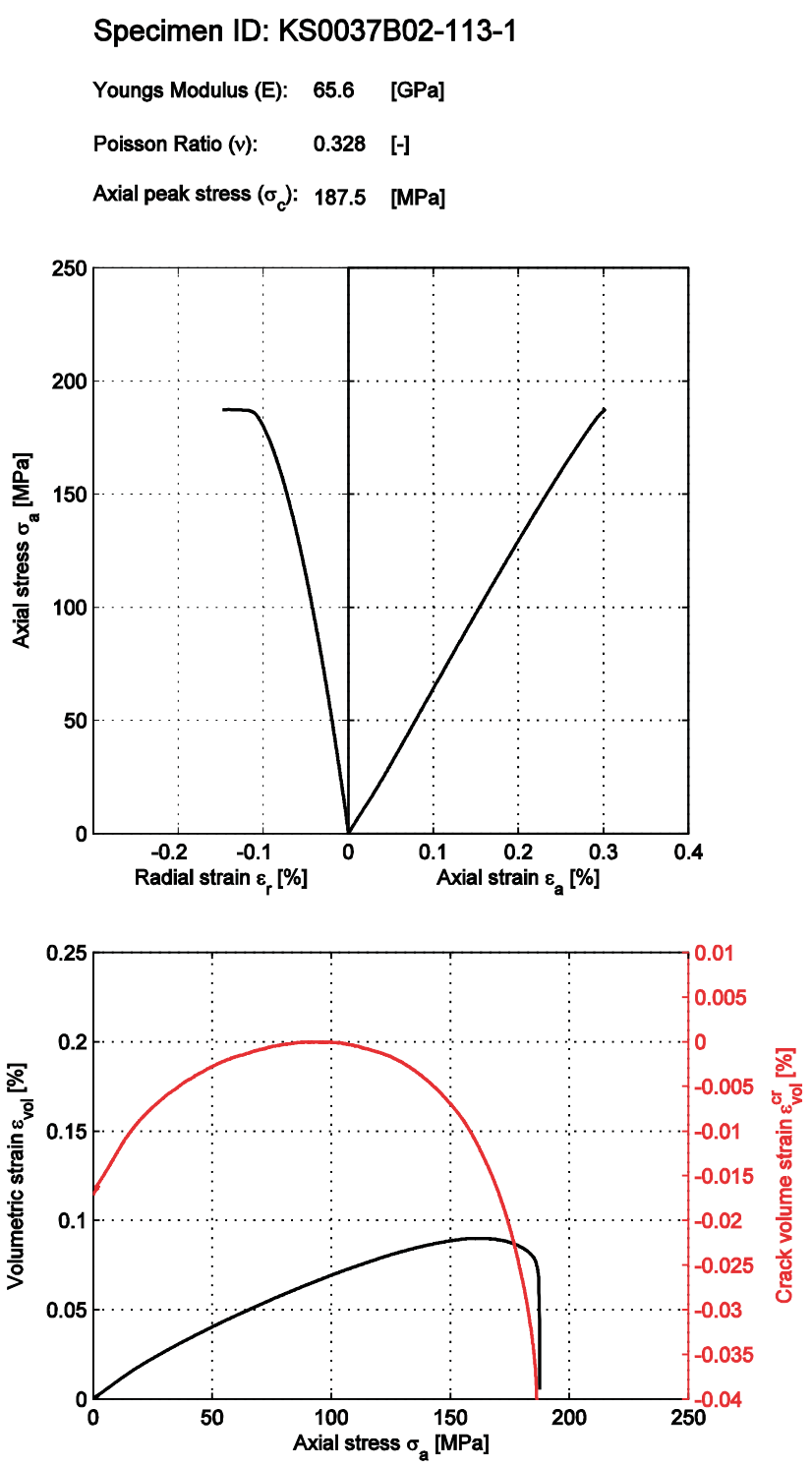

Figure A-4. *Specimen KS0037B02-113-1: Axial stress versus axial strain and volumetric strain versus axial stress.*

Specimen ID: KS0037B02-113-2

Before mechanical test

After mechanical test

Diameter (mm)	Height (mm)	Density (kg/m^3)
50.8	127.3	2780
Comments:	–	

Figure A-5. *Specimen KS0037B02-113-2: Photographs before and after testing, dimensions and measured wet density.*

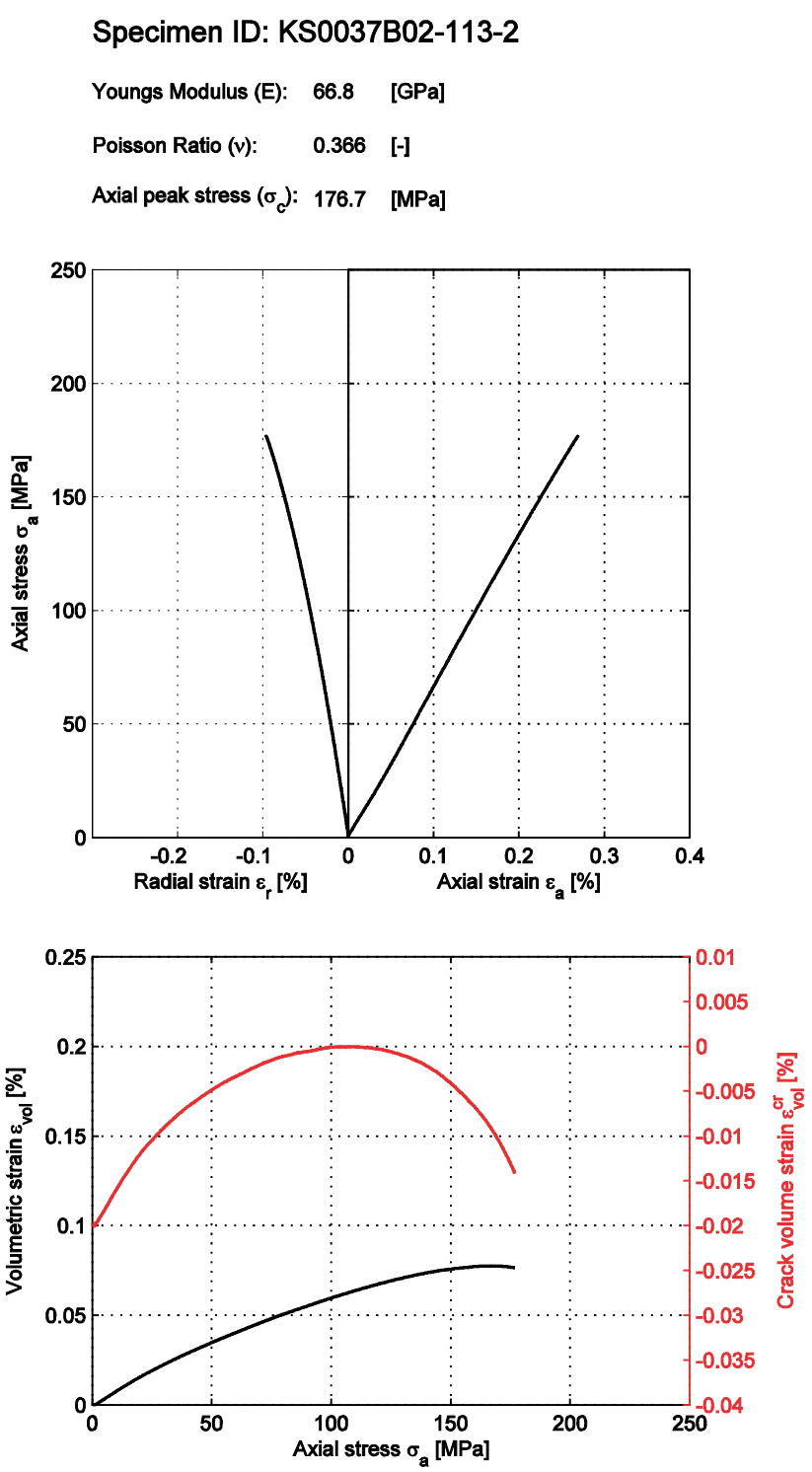

Figure A-6. *Specimen KS0037B02-113-2 (first loading): Axial stress versus axial strain and volumetric strain versus axial stress.*

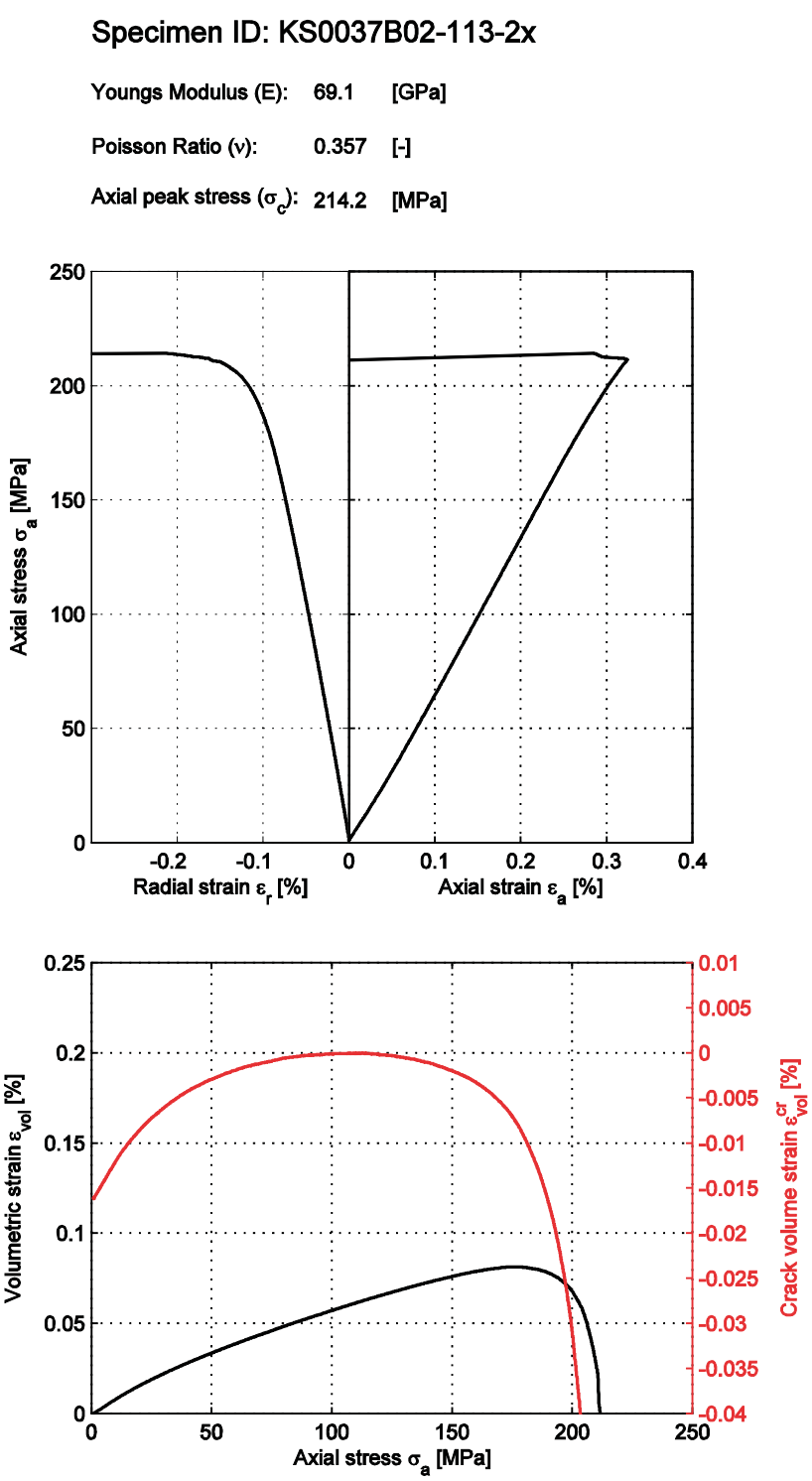

Figure A-7. *Specimen KS0037B02-113-2 (second loading): Axial stress versus axial strain and volumetric strain versus axial stress.*

Specimen ID: KS0037B02-113-3

Before mechanical test

After mechanical test

Diameter (mm)	Height (mm)	Density (kg/m^3)
50.8	114.4	2780
Comments:	–	

Figure A-8. *Specimen KS0037B02-113-3: Photographs before and after testing, dimensions and measured wet density.*

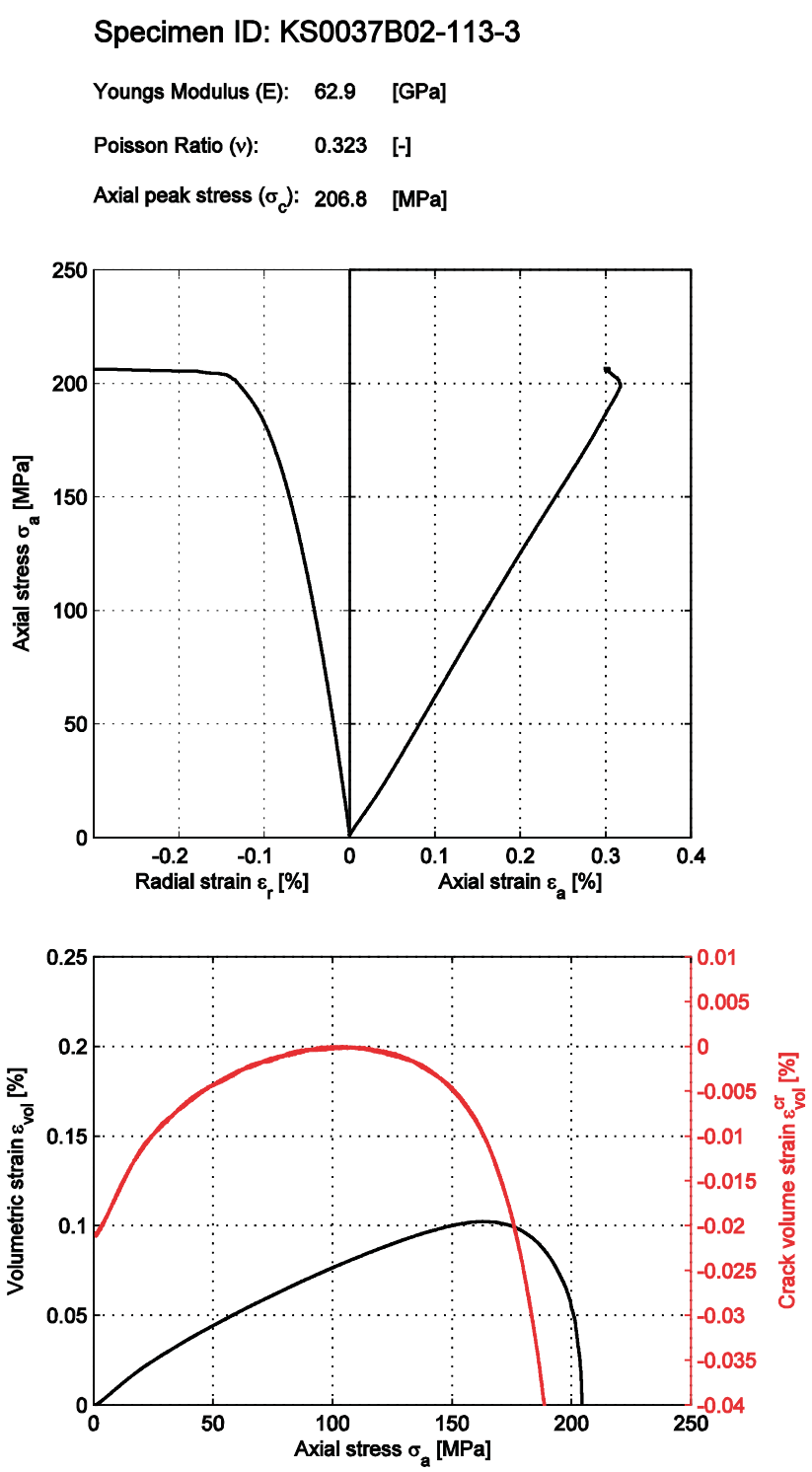

Figure A-9. *Specimen KS0037B02-113-3: Axial stress versus axial strain and volumetric strain versus axial stress.*

A.3.2 Acoustic emission measurements

AE-measurements were carried out during the test of KS0037B02-113-2. The graph showing the cumulative number of hits versus time is shown in Figure A-10. The mechanical test started 39 seconds after the AE sampling began.

It is seen that there are accumulation of activities during the micro crack closure part. The rate starts to drop at about 64 seconds (26 MPa). The decrease continues up to 92 seconds (54 MPa) where the accumulation rate becomes constant. It can be observed in Figure A-10 that there are some stronger signals at both 64 and 92 seconds. The accumulation rate of events begins to increase at about 170 seconds (132 MPa). The loading was stopped at 215 seconds and unloaded. The response looks similar to other uniaxial compression tests on diorite (Diederichs et al. 2004, Staub et al. 2004). The systematic crack initiation is starting on about 132 MPa. The loading was stopped before the crack damage stress level was reached.

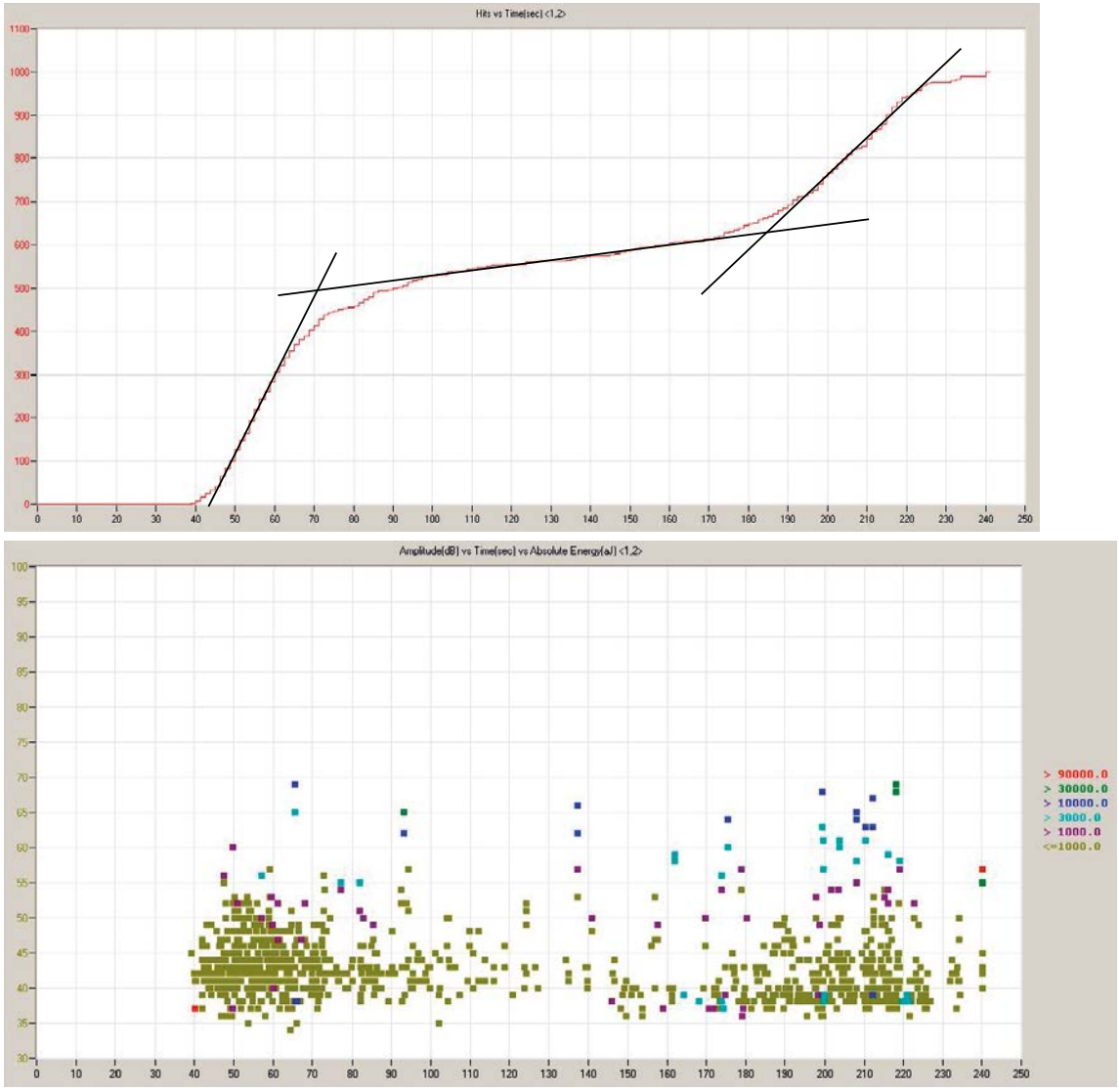

Figure A-10. *Upper graph: Cumulative of the number of hits versus the test time. Lower graph: Amplitude and absolute energy of the events versus the test time.*

A.3.3 Summary of results

The results from the density measurement and mechanical tests are summarized in Table A-2.

A comparison with other uniaxial compression tests carried out on Äspö diorite from Äspö HRL is shown in Table A-3.

It should be remarked that the evaluation method for the elasticity parameters differs between the test results presented in this report and for the results from Staub et al. (2004). The elasticity parameters is evaluated as the secant values between the axial stress levels at –0.01 % of radial strain and 50 % of peak strength in Staub et al. (2004). The effect on the values is shown in Table A-4. The Young's modulus is about 2 % higher and the Poisson ratio is about 12 % lower using the method in Staub et al. (2004) compared with the present data.

Table A-2. Summary of results.

Identification	ρ_{wet} (kg/m^3)	E (GPa)	v (–)	σ_{ci} (MPa)	σ_{cd} (MPa)	UCS (MPa)	σ_{ci}/ UCS	σ_{cd}/ UCS
KS0037B02-113-1	2770	65.6	0.33	98.2	161.4	187.5	0.52	0.86
KS0037B02-113-2	2780	66.8*	0.37*	109.1*	165.7*	–	0.51*	0.77*
KS0037B02-113-2x	2780**	69.1**	0.36**	111.8**	176.3**	214.2	0.52**	0.82**
KS0037B02-113-3	2780	62.9	0.32	107.6	164.3	206.8	0.52	0.79
Mean value	2777	65.1	0.34	104.9	163.8	202.8	0.52	0.81
Std deviation	6	2.0	0.02	5.9	2.2	13.8	0.01	0.05

* The parameters are evaluated using a UCS-value of 214.2 MPa.

** The parameters are not included in the calculations of the mean value and standard deviation.

Table A-3. Summary of results from different investigations on Äspö diorite.

Borehole	ρ_{wet} (kg/m^3)	E (GPa)	v (–)	σ_{ci} (MPa)	σ_{cd} (MPa)	UCS (MPa)	σ_{ci}/ UCS	σ_{cd}/ UCS	Eval. meth.*	Comment
KS0037B02	2777	65.1	0.34	105	164	203	0.52	0.81	VS	KS0037B02-113-1, -2, -3
KS0037B02	2780	66.8	0.37	132	–	214	0.62	–	AE	KS0037B02-113-2
KA3376B01**	2730	68.1	0.28	87.1	179	199	0.44	0.90	VS	From Staub et al. (2004)
KQ***	2755	75.8	0.27	96.3	199	216	0.45	0.92	VS	From Staub et al. (2004)
KQ***	2755	75.8	0.27	121	204	216	0.56	0.95	AE	From Staub et al. (2004)

* Evaluation of σci and σcd. VS = crack volume strain and volume strain, AE = acoustic emission.

** Mean value of two specimens.

*** Mean value of five specimens from boreholes KQ0061G01, KQ0064G07 and KQ0065G01.

Table A-4. Effect of different evaluation methods for determining the elasticity parameters.

Identification	E (SP) (GPa)	E (Staub) (GPa)	Rel diff E (%)	v (SP) (–)	v (Staub) (–)	Rel diff v (%)
KS0037B02-113-1	65.6	66.8	1.8	0.328	0.292	–11.0
KS0037B02-113-2	66.8	68.2	2.1	0.366	0.321	–12.3
KS0037B02-113-3	62.9	64.6	2.7	0.323	0.282	–12.7